The suction effect during freak wave slamming on a fixed platform deck: smoothed particle hydrodynamics simulation and experimental study

Peng-Nan Sun[a], Min Luo[b,*], David Le Touzé[a], A-Man Zhang[c]

[a] *Ecole Centrale Nantes, LHEEA Lab. (ECN and CNRS), Nantes 44300, France*
[b] *College of Engineering, Swansea University Bay Campus, Swansea SA1 8EN, UK*
[c] *College of Shipbuilding Engineering, Harbin Engineering University, Harbin 150001, China*

Abstract

During the process of wave slamming on a structure with sharp corners, the wave receding after wave impingement can induce strong negative pressure (relative to the atmospheric pressure) at the bottom of the structure, which is called the suction effect. From the practical point of view, the suction force induced by the negative pressure, coinciding with the gravity force, pulls the structure down and hence increases the risk of structural damage. In this work, the smoothed particle hydrodynamics (SPH) method, more specifically the δ^+SPH model, is adopted to simulate the freak wave slamming on a fixed platform with the consideration of the suction effect, i.e. negative pressure, which is a challenging issue because it can cause the so-called tensile instability (TI) in SPH simulations. Key to overcome the numerical issue is to use a numerical technique named tensile instability control (TIC). Comparative studies using SPH models with and without TIC will show the importance of this technique in capturing the negative pressure. It is also found that using a two-phase simulation that takes the air phase into account is essential for an SPH model to accurately predict the impact pressure during the initial slamming stage. The freak wave impacts with different water depths are studied. All the multiphase SPH results are validated by our experimental data. The wave kinematics/dynamics and wave impact features in the wave-structure interacting process are discussed and the mechanism of the suction effect characterized by negative pressure is carefully analyzed.

Keywords: smoothed particle hydrodynamics, δ-*plus*-SPH model, freak wave impact, suction effect, negative pressure, tensile instability

*Corresponding author.
Email addresses: sun.pengnan@ec-nantes.fr (Peng-Nan Sun), min.luo@swansea.ac.uk (Min Luo), david.letouze@ec-nantes.fr (David Le Touzé), zhangaman@hrbeu.edu.cn (A-Man Zhang)

1. Introduction

The study of the freak wave impact on marine structures is an important topic in ocean engineering. Freak waves possess tremendous destructive power and are unexpected. When impacting on ocean structures such as oil and gas platforms, the freak waves can lead to serious damage and instability to these structures. Recent disasters induced by the abnormally big waves include those happened in [25] and [26]. As the global climate changes, more extreme wave events are likely to happen with higher intensities. In this context, a good understanding on the extreme wave actions on platform structures are crucially important.

Substantial research works investigated the extreme wave impact on platform structures with the emphasis on different aspects such as the wave slamming loads [19, 20, 51, 50, 73] and the wave overtopping [21, 56, 13, 11]. An important phenomenon during the wave structure interaction process is the negative pressure (or suction effect) that was discussed by [19] and more recently by [51] and [50]. Indeed, the suction effect was observed in the wave interaction with breakwater as well [2]. Although the suction effect has been documented, it is not well understood. The questions that need more investigations include: 1) how the negative pressure is generated; and 2) what factors affect the magnitude of the negative pressure. This study aims to fill the knowledge gap by conducting experimental and numerical studies of freak wave slamming on a fixed platform deck.

To simulate the violent breaking wave impact on structures, a large number of computational fluid dynamics (CFD) solvers have been developed, and most of them are based on the mesh-based algorithms such as the finite difference method [32, 72] and the finite volume method [10]. In the last two decades, anther category of CFD solvers that have been attracting much interest is the particle method, which gets rid of meshes. The smoothed particle hydrodynamics (SPH) method [34, 68, 66, 67, 74] and the moving particle semi-implicit (MPS) method [23, 24] are two of the most widely used particle methods. Due to the mesh-less nature, the particle methods have distinct advantages in modelling violent breaking waves and the complex wave-structure interaction processes, which normally involve fluid fragmentation and coalescence [8].

However, in the published literature of SPH or MPS methods, most of the wave impact studies focused on positive impact forces on a structure while the suction effect and the associated negative pressure have been rarely studied in detail. Indeed, the accurate modelling of suction effects using SPH is not trivial since the negative pressure in the flow induces the tensile instability (TI) [47], under which the fluid particles lose the capability of self-adjusted regularity [62]. The TI further leads to the unphysical flows voids [43], the consequence of which will be the false evolution of the subsequent flow. In the water exit problems, for example, the fluid particles near the moving structure are stretched and fluid pressure becomes negative. In previous studies, the tensile instability and unphysical flows voids caused by negative pressure were

only concerned and addressed in the modelling of viscous flows around bluff bodies (see e.g. [57, 64]). However, for most fluid impact flows like freak waves slamming on fixed structures, very little attention was paid to the accuracy in negative pressure regions where suction effects take place.

To carefully study the suction effects in freak wave slamming flows, in the present work, we carried out a series of two dimensional (2D) experiments involving freak wave impact on a fixed rectangular deck platform. Freak wave impacts with different still water depths were tested. In these experimental tests, positive wave pressure occurs in the initial impact stage (the water-entry phase, as discussed in [19]). Subsequently, the wave flows recede from the platform under gravity, inducing negative pressures, i.e. the suction effect, at the bottom of the platform. Comprehensive measurements of wave elevation, wave velocity, breaking wave profile and wave impact pressure will be adopted to validate our numerical results.

In this study, we will adopt the recently developed δ^+SPH model [59, 62, 63] to simulate the freak wave slamming on a fixed platform deck, with the emphasis on the air cushioning effect during the water-entry phase and the suction effect during the water-exit phase. The multiphase SPH results will be thoroughly validated by the experimental data. We will show that the numerical technique of tensile instability control (TIC) in the δ^+SPH model plays an important role in preventing the TI and ensures an accurate SPH simulation of the whole precess of the freak wave slamming. The wave kinematics/dynamics and wave impact features in the wave-structure interacting process will be discussed and the mechanism of the suction effect characterized by negative pressures will be carefully analyzed.

The present work is organized as follows: Section 2 will be dedicated to the introduction of the δ^+SPH scheme and related numerical treatments for building a 2D wave flume; Section 3 will introduce the setup of the experimental campaign, the data of which will be compared with the SPH simulations; In Section 4, SPH results of the regular and freak wave generation and propagation will be validated; In Section 5, the freak wave impact on the fixed platform is studied through δ^+SPH simulations. The importance of simulating the air cushioning effect during the initial slamming stage and preventing the tensile instability in the region of strong negative pressure will be highlighted and detailed numerical and experimental results will be exhibited, compared and discussed; In Section 6, the effects of wet-deck clearance on the green water overtopping and impact force will be studied. Conclusions and future remarks will be presented in the last section.

2. The SPH model and numerical techniques for wave propagation and impact

The SPH models have been quite popular in the community of computational fluid dynamics for solving free-surface flows and/or fluid-structure interactions with large flow boundary movements or deformations. Among the most successful SPH models [33, 54, 49, 3, 29, 69, 76, 65], the so-called δ-SPH

model [38] is one representative variant that has been widely used for solving hydrodynamic problems in ocean engineering [55, 75].

The advantages of δ-SPH model include its strong capability in preventing pressure noise and the low numerical dissipation when the particle resolution is adequate. Therefore, δ-SPH model very suits the simulation of long distance wave propagation problems. However, when it is applied for flows around bluff bodies, e.g. viscous flows around rigid bodies [57], the unphysical flow voids generated by negative pressure become the obstacles for obtaining accurate solutions. Fortunately, the combination of δ-SPH with the particle shifting technique [33] and a tensile instability control (TIC) [62] leads to a new SPH variant δ^+SPH which overcomes the defect of the classic δ-SPH . Therefore, in the present work, the freak wave impact on structure with sharp corners will be investigated using the δ^+SPH model. Comparisons between δ^+SPH solutions with classic δ-SPH results and self-produced experimental data will demonstrate the improvement and accuracy of the new SPH model.

2.1. The δ^+-SPH model

The discretized governing equations of the δ^+-SPH model [59] are:

$$
\begin{cases}
\dfrac{\mathrm{d}\rho_i}{\mathrm{d}t} = -\rho_i \displaystyle\sum_j (\boldsymbol{u}_j - \boldsymbol{u}_i)\cdot\nabla_i W_{ij}\, V_j + \delta\, h\, c_{0i} \sum_j \mathcal{D}_{ij}\cdot\nabla_i W_{ij}\, V_j, \\[2ex]
\dfrac{\mathrm{d}\boldsymbol{u}_i}{\mathrm{d}t} = \boldsymbol{g}_i - \dfrac{1}{\rho_i}\langle\nabla p\rangle_i^{\mathrm{TIC}} + \dfrac{\alpha h c_{0i}\rho_{0i}}{\rho_i}\displaystyle\sum_j \pi_{ij}\nabla_i W_{ij}\, V_j\,, \\[2ex]
\boldsymbol{r}_i = \boldsymbol{r}_i^* + \delta\boldsymbol{r}_i\,, \qquad \dfrac{\mathrm{d}\boldsymbol{r}_i^*}{\mathrm{d}t} = \boldsymbol{u}_i\,, \qquad V_i = \dfrac{m_i}{\rho_i}\,, \\[2ex]
\delta\boldsymbol{r}_i = -CFL\cdot Ma\cdot h^2 \displaystyle\sum_j \left[2 + 2R\left(\frac{W_{ij}}{W(\Delta x)}\right)^n\right]\nabla_i W_{ij}\, V_j\,,
\end{cases}
\tag{1}
$$

where ρ_i, $\boldsymbol{u}_i$ and $\boldsymbol{r}_i$ denote the density, velocity and position associated with the particle indexed by i, respectively. $\boldsymbol{r}^*$ stands for the particle position obtained by integrating its physical velocity $\boldsymbol{u}$, but in δ^+SPH a shifting correction $\delta\boldsymbol{r}_i$ is added to $\boldsymbol{r}^*$ in each time step for obtaining the final regularized particle position. We note that, as the refining of the particle resolution, the particle repositioning vector $\delta\boldsymbol{r}_i$ converges to zero and therefore the particle trajectory converges to its Lagrangian trajectory [58].

The particle mass m is constant and the particle volume is evaluated as $V_i = m_i/\rho_i$. The kernel function $W_{ij} = W(\boldsymbol{r_i} - \boldsymbol{r_i}, h)$ is calculated between the particle pair indexed by subscripts i and j. The C2 Wendland kernel [71] is applied for all the simulations in this work with the smoothing length h equal to two times of the initial particle spacing Δx. Therefore, in the inner fluid region, each particle has about 50 neighboring particles. The gradient of the kernel function $\nabla_i W_{ij}$ is evaluated with respect to the position of particle i. $\boldsymbol{g}$ is the

gravity acceleration which is assigned as $-9.81\,m/s$ in all the simulations. We note that the pressure gradient term $\langle \nabla p \rangle_i^{\mathrm{TIC}}$ needs to be carefully determined using a tensile instability control (TIC) technique [62] in order to maintain numerical stability when pressure p becomes negative. This will be discussed in detail in Section 2.1.1.

In system (1) two diffusive terms are added to stabilize the numerical solution of density and velocity fields. According to [5], in the density diffusive term, $\mathcal{D}_{ij}$ is written as:

$$\mathcal{D}_{ij} = 2\left[(\rho_j - \rho_i) - \frac{1}{2}\left(\langle \nabla \rho \rangle_i^L + \langle \nabla \rho \rangle_j^L\right) \cdot \boldsymbol{r}_{ji}\right] \frac{\boldsymbol{r}_{ji}}{\|\boldsymbol{r}_{ji}\|^2}, \tag{2}$$

where $\boldsymbol{r}_{ji} = \boldsymbol{r}_j - \boldsymbol{r}_i$ and $\langle \nabla \rangle^L$ stands for the renormalized spatial gradient [53, 63]. In the velocity diffusive term [45], π_{ij} is written as

$$\pi_{ij} = \frac{(\boldsymbol{u}_j - \boldsymbol{u}_i) \cdot \boldsymbol{r}_{ji}}{\|\boldsymbol{r}_{ji}\|^2}. \tag{3}$$

In system 1, the diffusive parameters $\delta = 0.1$ and $\alpha = 0.02$ are adopted for all the test cases in this paper. Note that in a multiphase SPH simulation, the diffusive terms are set to zero if particles i and j are from different flow phases [63].

The pressure p is explicitly solved in the δ^+SPH model with an equation of state [4] as

$$p_i = B_i\left[\left(\frac{\rho_i}{\rho_{0i}}\right)^{\gamma_i} - 1\right], B_i = \frac{c_{0i}^2\,\rho_{0i}}{\gamma_i}. \tag{4}$$

The parameter γ is set as $\gamma_w = 7$ for water and $\gamma_g = 1.4$ for air [16]. Reference densities of water and air phases are $\rho_{0w} = 1000\,kg/m^3$ and $\rho_{0g} = 1.29\,kg/m^3$, respectively. In the simulation of water flows, according to the weakly-compressible hypothesis the density variation $\Delta\rho$ cannot exceed 1% of the reference density ρ_{0w}. This can be achieved by ensuring the Mach number less than 0.1 [46], i.e.

$$Ma = \frac{U_{max}}{c_w} \leq 0.1\,, \tag{5}$$

where c_w is the sound speed in water. As studied by [37], in the simulation of gravity wave propagations, U_{max} can be chosen according to the wave celerity c which is written as

$$c = \sqrt{gH\,\frac{\tanh(kH)}{kH}}, \tag{6}$$

where k denotes the wave number and H is the initial water depth. Since in most cases of the present work, shallow water waves are studied, i.e. H/λ approaches zero, λ is the wave length. In these shallow water cases, $\tanh(kH)$

approaches kH and therefore the wave celerity c approaches $\sqrt{gH}$ [4]. Therefore, the artificial sound speed c_w can be determined by

$$c_w \geq 10\,c \approx 10\sqrt{gH}. \tag{7}$$

The second factor for determining c_w is the maximum pressure p_{max} when water impact occurs [41]. The maximum density variation $\Delta\rho_{max}$ caused by the p_{max} should also be less than 1% of the reference density, i.e.

$$\Delta\rho_{max} \approx p_{max}/c_w^2 \leq 0.01\rho_{0w}. \tag{8}$$

Therefore, the artificial sound speed c_w of water can be finally determined as

$$c_w \geq 10\text{max}(\sqrt{gH}, \sqrt{\frac{p_{max}}{\rho_{0w}}}). \tag{9}$$

In order to take into account the physical compressibility of air phase, the sound speed for air is set as $c_g = 340\,m/s$ for all the multiphase cases in this paper.

As it can be seen in system 1, a particle shifting technique (see [33, 59] and [27]) is applied for repositioning particles, i.e. $\boldsymbol{r}_i = \boldsymbol{r}_i^* + \delta\boldsymbol{r}_i$. In the formulation of $\delta\boldsymbol{r}_i$, $n = 4$ and $R = 0.2$ is used based on the adopted kernel function and the smoothing length [59]. We note that, in a single-phase SPH simulation, the particle shifting vector $\delta\boldsymbol{r}_i$ needs a correction when the particle i has at least one neighboring particle on the free-surface. The shifting component along the normal directions to the free-surface is set to zero, while the tangential shifting is allowed, see more in [59]. For the multiphase case, the particle shifting near the air-water interface is treated with the technique proposed in [44, 28].

CFL is the Courant-Friedrichs-Levy coefficient for determining the time step Δt. The fourth-order Runge-Kutta integration method is used in the present SPH scheme because it allows a larger time step with *CFL* up to 1.25.

Finally, the time step Δt is determined as

$$\Delta t = CFL \cdot \min(\frac{h}{c_g}, \frac{h}{c_w}, \frac{h}{c_{g-w}}); \quad c_{g-w} = c_w\sqrt{\frac{\gamma_g\,\rho_{0w}}{\gamma_w\,\rho_{0g}}}, \tag{10}$$

where c_{g-w} is a newly defined sound speed by assuming $c_{g-w}^2\,\rho_{0g}/\gamma_g = c_w^2\,\rho_{0w}/\gamma_w$ which is a relation used in many multiphase SPH simulations (see, e.g., [16, 63]) to ensure numerical stability.

2.1.1. Tensile Instability Control

The pressure gradient term should be treated carefully in order to avoid tensile instability especially in cases with strong negative pressure [62]. Generally, in classic SPH models, the pressure gradient term in the momentum equation is written with the classic form using a pressure summation $(p_j + p_i)$. However, as suggested in [62] for a tensile instability control (TIC), the pressure gradient should be implemented in the following manner to completely prevent the occurrence of unphysical flow voids:

$$\langle\nabla p\rangle_i^{\text{TIC}} = \begin{cases} \sum_j (p_j - p_i)\nabla_i W_{ij}\,V_j & p_i \leq 0 \quad \text{and} \quad i \notin \mathscr{S}_F, \\ \sum_j (p_j + p_i)\nabla_i W_{ij}\,V_j & else, \end{cases} \tag{11}$$

where $\mathscr{S}_F$ denotes the particle set containing the free-surface and its neighbouring particles [59]. We note that, the pressure gradient with the summation form $(p_j + p_i)$ is important to ensure numerical stability of the free-surface because this form correctly enforces the dynamic free-surface boundary condition (see [48], [14] and [15]). The pressure gradient with the pressure difference $(p_j - p_i)$ is a non-conservative format which would lead to errors of the momentum conservation. To remedy this, the particle shifting technique is used to regularize particle positions, see in system 1. A uniform particle distribution after using the shifting helps to minimize the non-conservations of linear momenta.

2.2. Boundary conditions

In the present work, the "Fixed Ghost Particles" are adopted to model all the free-slip solid wall boundaries, including the walls in the SPH wave tank and the deck platform where the freak wave impacts occur. "Fixed Ghost Particles" consists of several layers of ghost particles. Through an extrapolation, SPH variables of the ghost particles are obtained based on the inner fluid. Generally, two different extrapolating methods are available in the literature. Marrone et al.[38] proposed to use the moving-least-square (MLS) interpolation which offers much higher accuracy (see e.g. [39]) but some mirrored interpolating points need to be arranged within the fluid layer close to the boundary. This brings difficulty when dealing with irregular boundary shapes. In this work, we have adopted the second method, i.e. the Shepard interpolation as proposed in [1]. This method is straightforward, free of using interpolating points, while is able to achieve satisfactory accuracy in modelling free-slip boundary conditions simply by omitting the viscous stress between fluid and ghost particles.

2.3. Wave making and wave absorbtion

In wave generation, different wave makers have been used, including the piston-type wave maker (more suitable for relatively shallow water), the flap-type one (for relatively deep water) or a combination of these two [4]. Owing to the Lagrangian nature, the SPH is able to simulate the physical motions of wave makers, which is especially advantageous in reproducing the laboratory cases of large waves. In the present SPH model, the wave makers are modelled by the aforementioned "Fixed Ghost Particles". The motions of the wave makers are enforced with the same paddle motions as used in the wave flume experimental campaign.

To prevent the undesirable wave reflection, a viscous damping zone is added at the downstream end of the numerical wave flume [70]. The damping zone has very high artificial viscosity and dissipates the kinetic energy of a fluid particle when it goes into this region. In this work, the artificial damping coefficient α in the second equation of system 1 is adopted to be 0.6 for the particles in the damping zone. The length of the damping zone equals to two times of the wave length.

Spurious pressure waves are often generated by the weak compressibility of fluid in SPH simulations of water entry or wave slamming problems [60, 61]. To

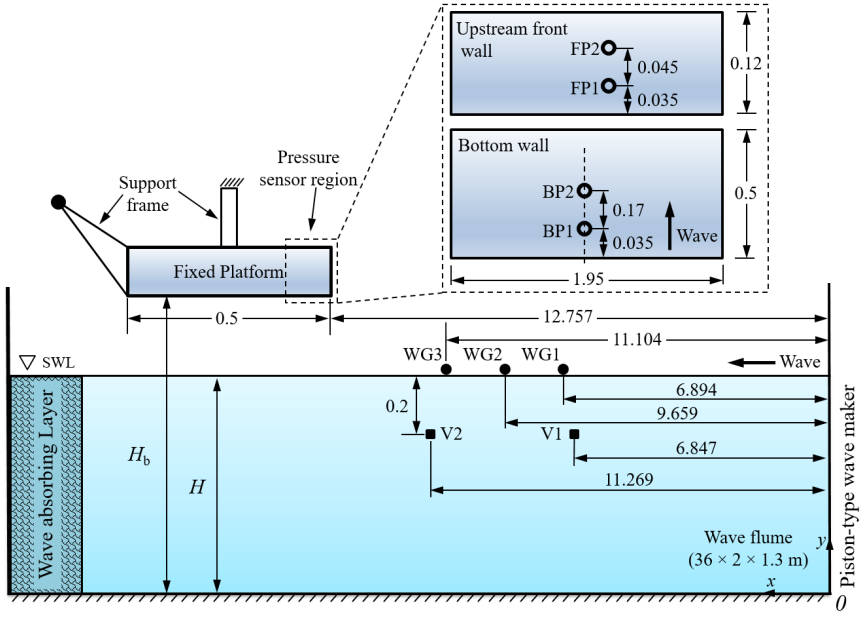

Figure 1: Sketch of the experimental setup for the test cases of freak waves impact on a fixed platform deck [35, 73] including details of the wave flume, horizontal locations of the platform, the wave gauges and the ADV probes, and distributions of the pressure sensors on the deck platform.

prevent the reflection of these spurious pressure waves from the fluid bottom, a sponge layer [22] with the thickness of $0.1H$ and length of $5L$ (L is the platform length) has been arranged along the fluid bottom beneath the deck platform.

3. Experimental setup for freak wave generation and impact

Freak wave impacts on a fixed platform deck will be numerically studied using the δ^+SPH scheme introduced in the previous section. To validate the SPH results, experimental studies were carried out. The experimental setup used is similar to that adopted in [35] and [73]. The experimental data of a freak wave case was used to validate a numerical model called the Consistent Particle Method in [35], while in [73] the spatial distribution of the wave impact pressure on the platform was focused with the experimental data serving as a supplement to the immersed boundary method (IBM) simulation. In these two studies, only freak wave cases of water depth $H = 0.7\,m$ were studied. And in general, the numerical simulations in both studies did not fully reproduce the wave kinematics and dynamics during the wave impact process especially that the negative pressure during the wave receding stage was not accurately predicted. This study aims to simulate the negative pressure that has seldom been tackled in the particle method community. As will be shown later, the present δ^+SPH

produces superior results owing to its high accuracy in handling breaking wave slamming and negative pressure. One freak wave case of $H = 0.7\,m$ that has been presented in [35] and [73] is simulated and presented in Section 5.3.3. To examine the characteristics of wave impact in different water depth conditions, two more experimental cases of different water depth, i.e. $H = 0.65\,m$ and $H = 0.67\,m$, are studied in this study. Another new feature of the present experimental study is the measurement of wave velocities by the Acoustic Doppler Velocimetry (ADV).

For completeness of the illustration, the experimental setup is briefly introduced. As sketched in Figure 1, a rectangular platform of $1.95\,m$ in width, $0.12\,m$ in height and $0.5\,m$ in length, mimicking the deck of fixed marine structures, was suspended from the top and horizontally placed. The distance between the right (upstream) side of the platform to the home position of the wave maker is $12.757\,m$ and the height from the flume bottom to the platform bottom is H_b ($H_b = 0.7485\,m$ for all the cases except for Section 6). The platform spans almost the entire width of the wave flume with only a narrow gap ($2.5\,cm$) at each side wall for ease of installation. The influence of the gaps on the overall wave motion is marginal and localized, and hence the wave motion and action near the middle of the wave flume are not affected. Therefore, the two-dimensional SPH simulations are conducted in this study to save computational time.

Wave elevations were measured by three wave gauges, respectively named WG1, WG2 and WG3, with distances of $6.894\,m$, $9.659\,m$ and $11.104\,m$ to the home position of the piston wave maker. Wave velocities at two typical locations were measured by ADV probes, locating at the horizontal distances of $x_{v1} = 6.847\,m$ (V1) and $x_{v2} = 11.269\,m$ (V2) and at elevation of $d_v = 0.2\,m$ downward the still water level. This is a new measurement that has not been conducted in [35] and [73] (which used a similar experimental setup). Four pressure sensors were installed on the platform with two on the upstream front wall that faces the approaching wave (FP1 and FP2) and another two on the bottom wall (BP1 and BP2). The locations of the pressure sensors are shown in Figure 1. A high speed camera was used to record the wave profile evolution during the wave slamming process.

In the experimental campaign, we measured the actual paddle motion, wave elevations, wave velocities and wave impact pressures. All these signals were recorded and stored by an oscilloscope, and hence all these data are synchronized. We used the measured paddle motions as the inputs for numerical simulations. Hence the laboratory and numerical wave paddles move in exactly the same manner and we know the starting time point. In this way, the synchronization between the numerical and experimental results of wave elevations and impact pressures are achieved automatically.

For the experimental wave profile that was captured by a high speed camera, the synchronization with the numerical results was obtained by comparing the numerical wave profiles. Given the sampling frequency of the high speed camera (1000 Hz) and the sequential experimental image number, we know the time interval between any two images. We selected three experimental images during

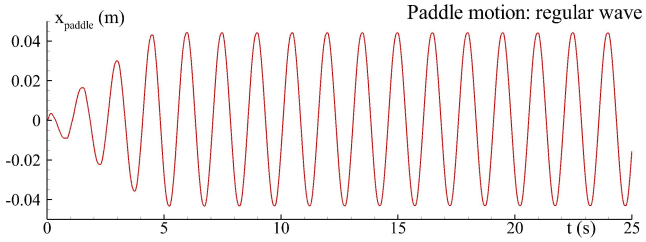

Figure 2: Horizontal motion of the paddle for generating a regular wave at still water depth $H = 0.5\,m$ (Supplementary data for this figure can be found in Section 8)

.

the wave-structure interaction process. We then chose the numerical snapshot (the time is known) that has a very similar wave profile (by eye) to the first experimental image and assume they are of the same timing. Followed, we produce two numerical snapshots that have the same timing as the other two experimental images. If the experimental and numerical wave profiles at both time instants are very similar, we say they are synchronized. If not, we repeat the same procedure to find the right timing for the experimental wave profile. Regular and freak waves with different still water depths were tested in the experiment and are simulated by the δ^+SPH model, which will be elaborated in the following sections.

4. Wave generation and propagation

Before the study of wave-structure interaction, it is crucially important to verify the accuracy of the present SPH model in generating waves without unphysical dissipations and undesirable reflections. In this section, both regular and freak waves are simulated with the δ^+SPH model. SPH results are validated with the experimental measurements and the solutions by the Boundary Element Method (BEM) in [12].

4.1. Regular waves

A regular wave case of initial water depth $0.5\,m$, wave period $1.5\,s$ and wave height $0.1\,m$ is firstly simulated with the paddle motion shown in Figure 2. Three different particle resolutions, respectively $H/\Delta x = 100$, $H/\Delta x = 50$ and $H/\Delta x = 25$, are adopted to test the particle-size convergence of the SPH model.

The wave elevations measured at the three wave gauge locations are plotted in Figure 3 where the SPH results, experimental data and the results of a BEM based potential flow solver are compared. At the lowest resolution, i.e. $H/\Delta x = 25$, the wave elevations predicted by the SPH are evidently smaller than the experimental data and the BEM results, especially at the location further away from the wave maker location. As the resolution refines, the accuracy of SPH results increases. Particularly, the numerical results

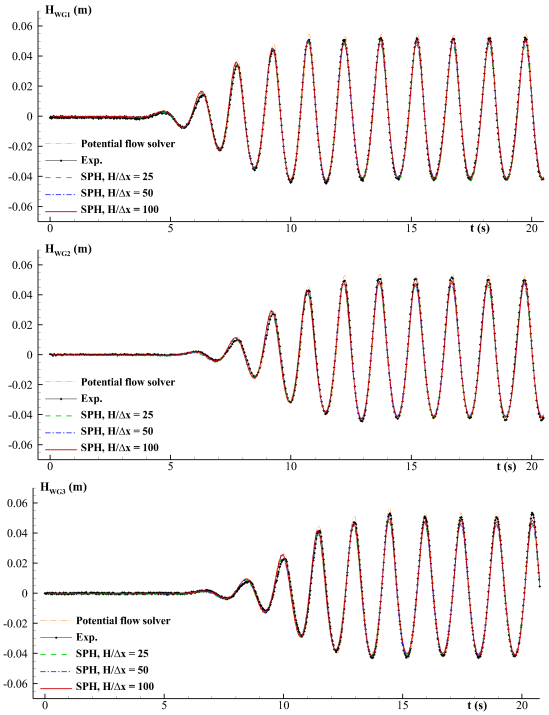

Figure 3: SPH results compared with solutions of a potential flow solver and experimental measurements for the regular wave elevations at the three wave gauges.

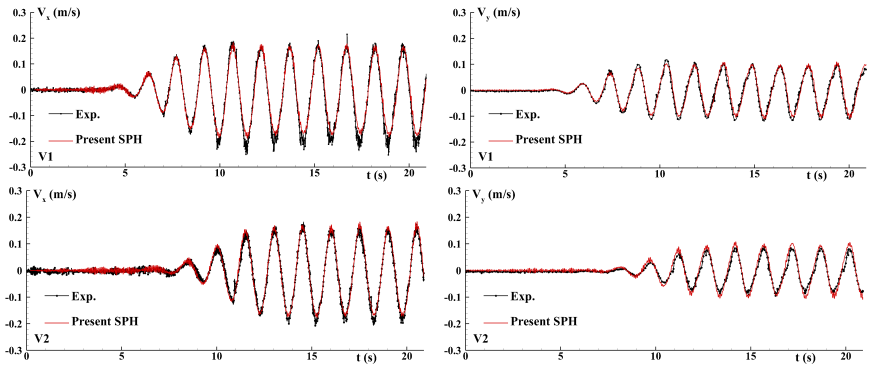

Figure 4: Comparisons between the SPH results with particle resolution $H/\Delta x = 100$ and experimental data for velocity components measured at the two probes (V1 and V2, see Section 3) in regular waves.

of $H/\Delta x = 50$ and $H/\Delta x = 100$ are quite close and agree well with the experimental and BEM results. This shows the particle-size convergence of the present SPH model. As discussed by [4], four particles are the minimum in the wave height to accurately resolve the wave propagation. In the present case, the wave height is $0.1m$ which consists of about 20 particles at the particle resolution of $H/\Delta x = 100$.

The present SPH model is further validated by comparing the wave velocity, which is a more challenging parameter to predict by a numerical model. To that end, time evolutions of the horizontal and vertical components of the velocities measured at V1 and V2 (see Figure 1), are plotted in Figure 3 where SPH results and experimental data are compared. Again, the SPH model captures the periodic wave velocities well without noticeable amplitude decay and phase lag. It means that this model introduces negligible unphysical dissipations, which is a remarkable advantage in the simulation of wave propagation in a relatively long domain. The numerical and experimental results also show that the horizontal velocity has a obviously larger amplitude than the vertical velocity, which is consistent with the fluid trajectory described by the wave theory in relatively shallow water ($kH = 1.112$).

4.2. Freak waves

After the test of a regular wave, the freak wave generation in a water domain of depth $H = 0.65\,m$ is studied in this section. The freak wave is generated based on the focused wave theory that describes the wave-wave interaction of a modulated wave packet. The characteristic wave length and wave period are $\lambda = 3.312\,m$ and $T = 1.563\,s$, respectively. More details of this theory are referred to [9, 36, 73]. For the studied case, the theoretical wave focusing position, at which all the wave crests happen, is specified to be $x = 12.45\,m$. The actual focusing location is slightly shifted due to the high nonlinearity of the focused wave, but the shift is not too much. After the occurrence of wave focusing, the large wave involves into a plunging wave. This enables

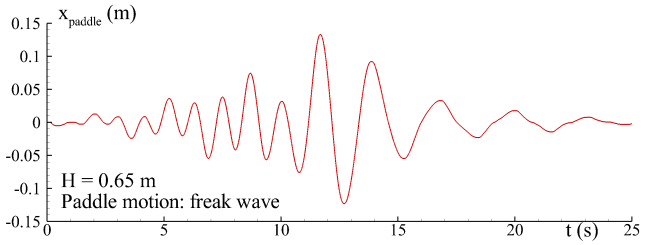

Figure 5: Horizontal motion of the paddle for generating a freak wave at still water depth $H = 0.65\,m$ (Supplementary data for this figure can be found in Section 8)

.

the generation of a large-amplitude non-breaking or slightly-breaking wave just before the wave impact happens. The measured paddle motion of this wave case is shown in Figure 5. Three different particle resolutions, respectively $H/\Delta x = 100$, $H/\Delta x = 50$ and $H/\Delta x = 25$, are adopted in the SPH model.

Wave elevations predicted by the SPH scheme are compared with the experimental measurements in Figure 6. The wave elevation at WG3 manifests a sudden appear of a very high wave of amplitude reaching $0.19\,m$. This is induced by the concurrence of a number of wave crests in the wave packet and is an unique feature of the "freak" wave. Owing to the high accuracy and low dissipation, the present SPH model is able to capture the highly-nonlinear wave.

SPH results of wave velocity with particle resolution $H/\Delta x = 100$ are plotted in Figure 7, in comparison with the experimental data. In general, the SPH model reproduces the velocities, that exhibit large amplitudes and rapid changes, very well. Some troughs in the experimental curves show fluctuations. Each trough corresponds to the instant when a wave trough occurs. In this situation, the measuring probes of the ADV are close to the free surface, which introduces some experimental noises that lead to the fluctuations.

5. Kinematics and dynamics during freak wave impact

5.1. Convergence of the plunging wave profile and impact pressure

In the focused wave case discussed above, after the wave packet passes the wave focusing location, the wave crest further develops into a plunging wave that impinges onto the platform structure (the experimental snapshots will be shown in Section 5.3). Adequate particles are needed to reproduce the large-steepness plunging wave. In addition, the impinging jet that impacts on the structure may be of small thickness. To accurately predict the impact pressure, a sufficient number of fluid particles is needed in the impact region. In Section 4, we have shown that a resolution of $H/\Delta x = 100$ successfully predicts the wave elevations and velocities at locations upstream the structure, where the wave exhibits some nonlinearities but not as much as the plunging wave just in front of the platform. For the same resolution, the predicted plunging wave crest does not show a clear lune shape, as show in Figure 8. This is because, in

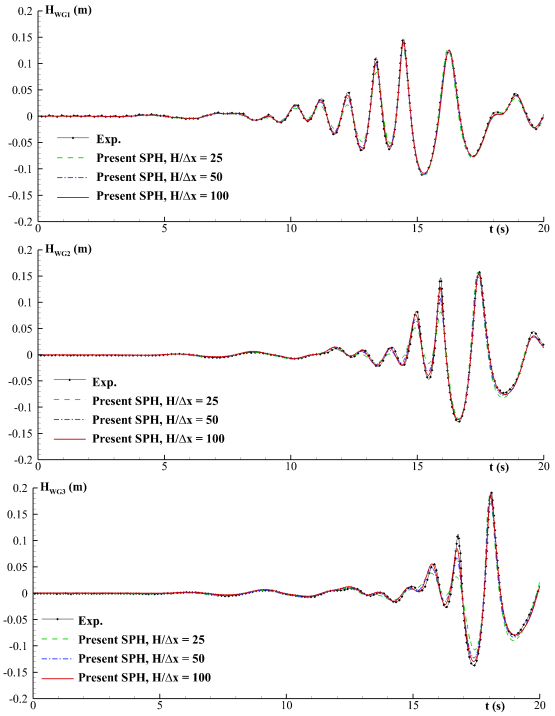

Figure 6: SPH results and experimental measurements for the freak wave elevations at three wave gauges.

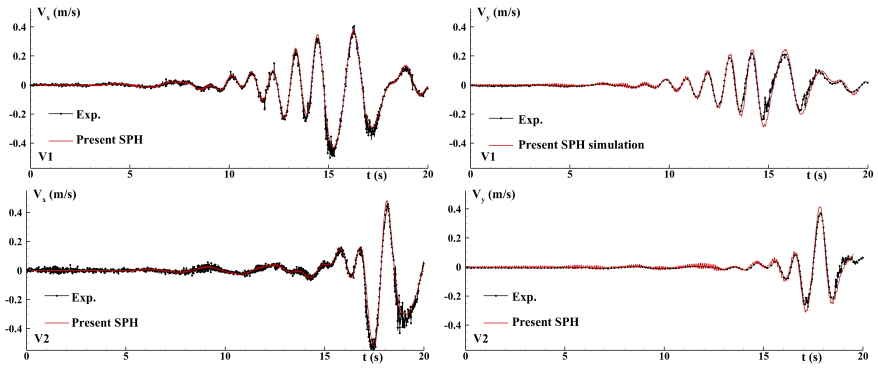

Figure 7: SPH results and experimental measurements for horizontal and vertical components of the velocities measured at two ADV probes (V1 and V2, see Section 3) in freak waves.

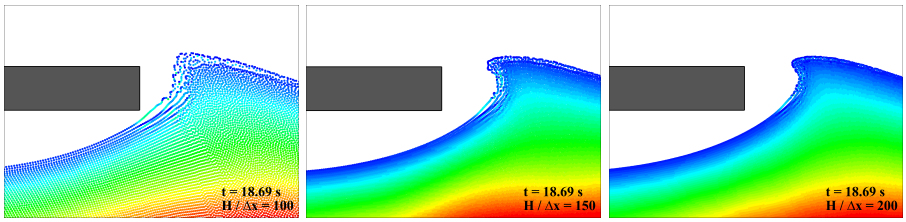

Figure 8: Snapshots of the wave profile before wave impact occurs: comparison between the SPH results of three particle resolutions: $H/\Delta x = 100$ (left), $H/\Delta x = 150$ (middle) and $H/\Delta x = 200$ (right).

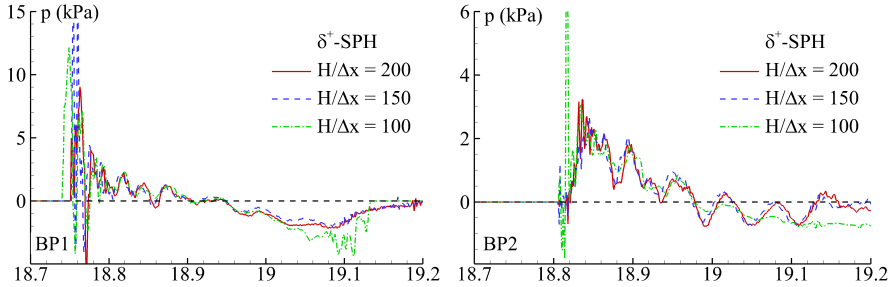

Figure 9: Wave impact pressures at BP1 and BP2 predicted by the δ^+SPH model and their variations with particle resolution.

this resolution, there are not enough particles to construct the high-curvature wave shape. A refined particle resolution, i.e. $H/\Delta x = 150$, leads to a very different wave profile that matches the experimental snapshot better as we will show later. Further increasing the resolution to $H/\Delta x = 200$ yields a slightly clearer free surface with less unphysical serration, but the shape of the wave profile is very close to that predicted by $H/\Delta x = 150$.

The plunging wave impinges on the platform structure and then recedes from the structure, which induces large impact and suction pressures. The pressures on the bottom (i.e. BP1 and BP2) walls of the platform and their variations with the particle resolution are presented in Figure 9. At both measurement locations, in general, the pressure results with $H/\Delta x = 150$ and $H/\Delta x = 200$ are close, with which the results of $H/\Delta x = 100$ show clear differences. Note that pressure fluctuations are observed at the initial slamming stage. These primarily stem from the weak-compressibility nature of the SPH method, which will be investigated in detail in Section 5.2.1.

In addition to the large wave impact pressure, the green water overtopping may cause serious serviceability issues to the facilities on the upper deck of the platform and hence is another problem concerned in marine structure design. We define the total volume (per unit width) of the water particles right above the top surface of the deck as the green water volume (indicated as V_G). In SPH calculations, $V_G = \sum_j V_j$ where j belongs to those particles who satisfy $13.257 > x_j > 12.757$ and $y_j > (H_b + 0.12)$. Figure 10 shows the

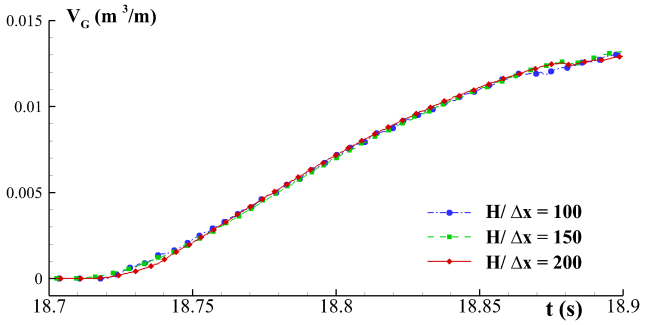

Figure 10: Green water volume predicted by the δ^+SPH model and the variation with particle resolution.

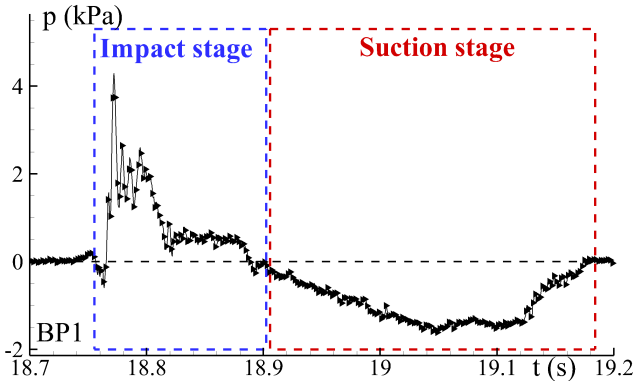

Figure 11: Experimental wave impact pressure at BP1 for the plunging wave impact case of water depth $H = 0.65\,m$; The impact and suction stages are defined based on the sign of the pressure value.

predicted volume of green water with different particle resolutions. The δ^+SPH simulations with the three particle resolutions predict almost identical green water volumes. This further shows the numerical results are converged at the particle resolution of $H/\Delta x = 200$.

The results of plunging wave profile, impact pressure and green water volume demonstrate good convergence properties of the SPH scheme. The resolution of $H/\Delta x = 200$ is sufficient for the simulation of the freak wave impact and therefore is adopted in the following simulations unless otherwise stated.

5.2. Key factors affecting the SPH simulation of freak wave slamming

The wave slamming process is divided into the impact and suction stages according to the sign of the wave impact pressure at BP1, as shown in Figure 11. In the following two subsections, the influence of the air phase on the wave impingement characteristics at the impact stage and the influence of the TIC scheme on the negative pressure at the suction stage will be studied.

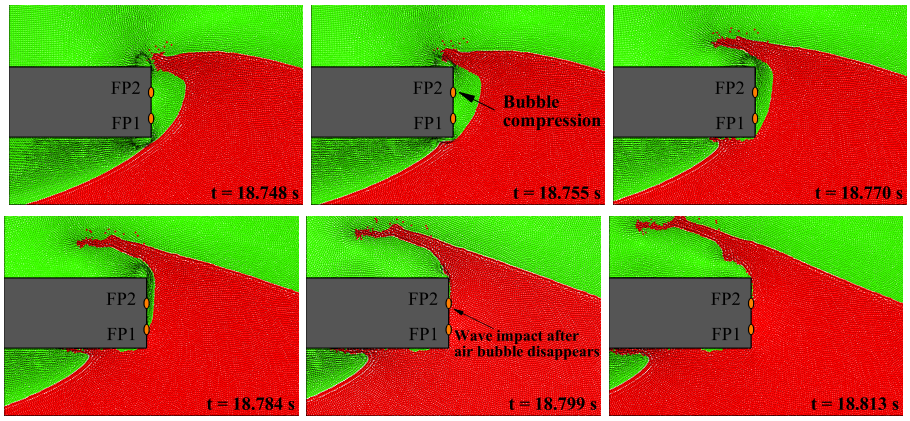

Figure 12: Snapshots of multiphase SPH results consisting of bubble compression and wave impact in the impact stage of the case with initial water depth $H = 0.65\,m$.

5.2.1. Influence of air phase on SPH results during the impact stage

The freak wave impinges on the front wall and entraps some air, which plays an important role in affecting the wave impact characteristics. Because of the high numerical complexity, however, very few particle simulations have considered the air phase in the freak wave slamming scenarios. In this section, a multiphase SPH simulation of the freak wave case of $H = 0.65\,m$ is conducted. The focus is on how the air phase media influences the numerical results during the impact stage when air entrapment exists. The evolvements of the wave profile are presented in Figure 12. The plunging wave crest arrives at the upstream vertical wall of the structure at $t = 18.748\,s$ and entraps an air bubble between the wall and the wave. The incident wave pushes and hence compresses the air bubble (see the snapshots from $t = 18.755\,s$ to $t = 18.77\,s$), during which process the pressure in the air bubble should increase to a certain level. The air in the bubble escapes rapidly from the gaps near the structure edges, as depicted by the velocity fields in the snapshots of $t = 18.77\,s$ and $t = 18.784\,s$. Eventually, the bubble disappears and the main body of the incident wave impinges on the front wall again, inducing another impact peak. The multiphase δ^+SPH model successfully predicts the pressure increase during the bubble compression and the second impact peak upon the disappearance of the bubble, as presented in the top panel of Figure 13. And in general, the predicted pressure results on both the front and bottom walls does not show evident unphysical oscillations.

In contrast, the impinging pressures produced by the single-phase δ^+SPH manifest large oscillations. In the absence of the air bubble that acts as a buffer between the incident wave and the structure, the water wave impacts on the front wall with a much larger velocity, which leads to a pressure impulse with excessive peak. Because of the weakly-compressible nature of SPH, the excessively-intense impingement causes excessive acoustic waves, which are radiated to the water wave and evolve into rarefaction waves with large negative pressure after interacting with the free-surface. This explains why pressure

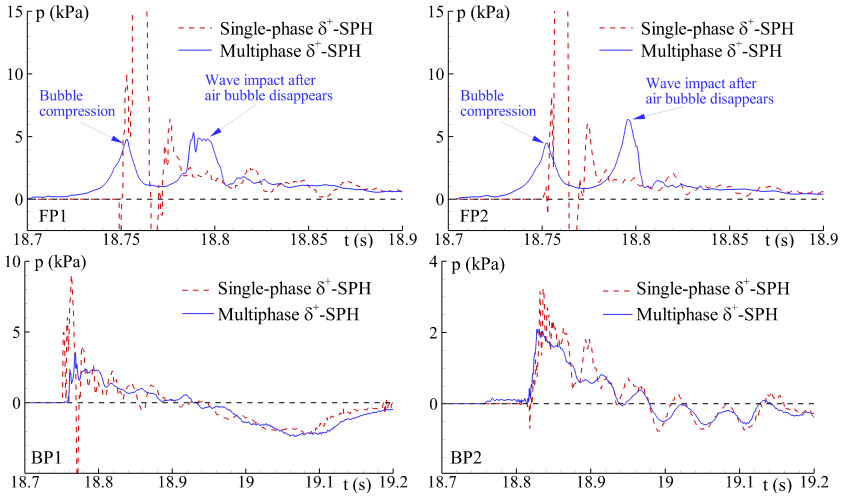

Figure 13: Comparison between the results of single-phase and multiphase δ^+SPH models for the wave impact pressure in the case of initial water depth $H = 0.65\,m$.

oscillations (acoustic waves) and negative pressures (rarefaction waves) appear after the positive peak in the single-phase SPH results. Similar observations of pressure oscillations have been documented in the numerical study of [40] and the experimental study of [31].

Indeed, as pointed out by Cooker [17] and Marrone et al. [40], when the weakly-compressible hypothesis is satisfied, the solution of a compressible flow impact can be equivalent to the combination of the solution of an incompressible fluid and an acoustic part. In δ^+SPH simulations, the acoustic waves can be dissipated by the diffusive terms. Therefore, the solving for weakly-compressible fluids converts to that for incompressible flows. From Figure 13, one may find that after a short period when all the acoustic waves are dissipated (after $t = 18.81\,s$), the single-phase and multiphase SPH results coincide with each other. This is because both the single-phase and multiphase solutions converge to the equivalent incompressible solution at this stage. The dissipation rate of acoustic wave is closely related to the sound speed. Specifically, a lower Mach number (i.e. large sound speed) leads to a quicker dissipation that is desirable. However, this will require a smaller step [40] and a finer particle resolution [30], both of which increase the computational cost. On the balance of numerical accuracy and efficiency, the Mach number of 0.1 is adopted in this study.

Because of the capturing of the air cushioning effect, the multiphase SPH model predicts more realistic wave impacts that are less intense than that produced by the single-phase SPH simulation and hence fewer acoustic waves are radiated after the wave impingement. Besides, with air particles outside the water surface, acoustic pressure waves from the water domain can be partially transmitted to the air domain and then dissipated, the consequence of which is that fewer rarefaction waves are reflected to the water domain. Moreover, the inclusion of air particles avoids the kernel truncation near the thin water

jet that happens in a single-phase simulation, thereby increasing the numerical accuracy. Owing to these features, the multiphase SPH simulation predicts more realistic pressures that have less unphysical fluctuations and avoid the unphysical negative pressure subsequently following the positive pulse peak. Through the above analysis, three conclusions are drawn:

- The air phase plays an important role at the initial stage of the wave slamming on the upstream vertical wall. The compression of the entrapped air bubble leads to the first pressure impulse. The escape of air in the entrapped bubble corresponds to the pressure decrease after the first pressure peak. After that, the wave impact following the collapse of the entrapped air bubble leads to the second pressure impulse.

- The multiphase SPH simulation gives more stable pressure results with less spurious fluctuations in the impact stage.

- The single-phase and multiphase SPH models give very similar results for the pressure evolutions in the suction stage.

5.2.2. Influence of TIC on SPH results during the suction stage

After the wave impingement, the wave tends to recede from the box-shape structure, which resembles the water-exit process. In reality, the wave recede induces negative pressures, i.e. suction, on the bottom wall of the structure. Unfortunately, it has been a challenge for SPH to model the negative pressure because of the tensile instability [47, 52, 40]. Within the authors' knowledge, very few SPH studies have addressed the suction effect during the wave slamming process up to now. From the practical point of view, however, the accurate prediction of negative pressures on a platform structure is crucially important as the negative pressures will act as a suction that pulls the platform down and increase the risk of structural collapse. This section, therefore, will investigate the capability of the δ^+SPH model equipped the TIC technique to handle the negative pressure.

Based on the plunging wave case of the still water depth $H = 0.65\,m$, we carried out two SPH simulations by using the traditional δ-SPH model without TIC [38] and the δ^+SPH model with TIC [62]. The wave snapshots with pressure contour produced by the two SPH models are depicted in Figure 14. In general, both SPH models predict smooth pressure fields. This is largely attributed to the density diffusive term added in the continuity equation (the key concept of the δ-SPH model).

Here we only focus on the pressure evolution in the suction stage. After the wave hits the platform, it propagates with its pathway blocked by the structure. Hence the water has to divert: the upward part becoming green water and the downward part going into the main water body (see both the snapshots at $t = 19.00\,s$). When water passes through the bottom corner of the platform, a small wake region is generated at the downstream side near the structure corner, in which the fluid pressure can be negative (relative to the atmospheric pressure). The negative pressure is successfully reproduced by the δ^+SPH model

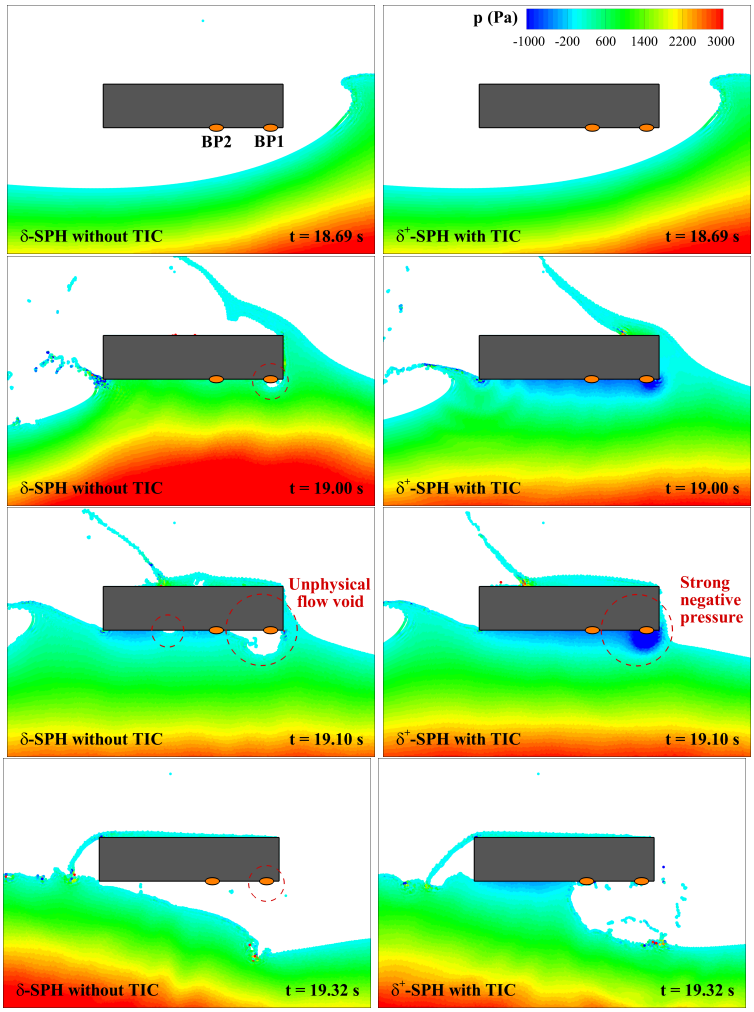

Figure 14: Comparison between the numerical results of the δ-SPH without TIC (left column) and the δ^{+}SPH with TIC (right column); To clearly demonstrate the negative pressure, the minimum pressure value in the legend has been adjusted to $-1000\,Pa$.

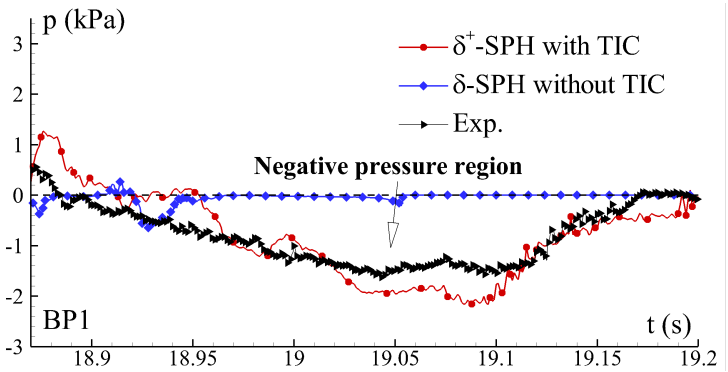

Figure 15: Pressure at BP1 on the platform bottom during the suction stage. Experimental data is compared with results of the δ-SPH without TIC and the δ^+SPH with TIC.

with TIC (see the snapshots at $t = 19.00\,s$ and $t = 19.10\,s$ in the right column of Figure 14) and it keeps for some time with the fluid sticking to the platform bottom. With the propagation of the wave, the fluid-structure interface reduces due to wave receding (see the snapshots at $t = 19.32\,s$ by the δ^+SPH).

In the traditional δ-SPH simulation, however, the negative pressures are not predicted. This further leads to unphysical voids in the region where negative pressures should actually happen (see the left figure of $t = 19.10\,s$). Therefore, the predicted wave profiles show significant differences to those predicted by the δ^+SPH model. In the δ-SPH simulation, the location of BP1 gets emerged (no water sticks to it) from $t = 19.00\,s$ and hence the pressure at this location becomes zero from this time instant. The subsequent snapshots produced by the δ-SPH model shows a complete detachment of the fluid from the platform bottom (see $t = 19.32\,s$). The phenomena of flow voids and the fast detachment of fluid from the structure are unphysical and do not match the experimental observations as described by [6].

For a further illustration, the pressure histories at BP1 predicted by the two SPH models are compared with the experimental data during the suction stage in Figure 15. As can be seen, the recorded negative pressure has a magnitude of around 1.6 kPa, which is more than 1/3 of the maximum positive pressure as shown in Figure 11. This means that large negative pressures do happen in the suction stage of a wave slamming process. The negative pressure is difficult to simulate as it induces unphysical voids and/or fragmentations of the fluid [40]. Because of this, the traditional δ-SPH produces spurious zero pressures at BP1 during the suction stage. In contrast, the δ^+SPH predicts the negative pressures very well owing to the capability of the TIC technique in dealing with negative pressure. This shows the advantage of the δ^+SPH model. Therefore, the δ^+SPH model with TIC is adopted in the simulations from here on in this study.

5.3. Wave profile and impact with different still water depth

In addition to the freak wave case of water depth $H = 0.65\,m$ as presented above, two more cases with water depths of $H = 0.67\,m$ and $H = 0.7\,m$ are

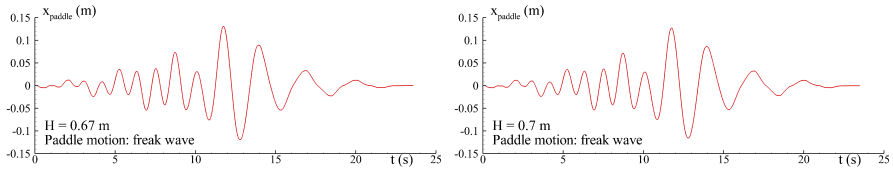

Figure 16: Horizontal motions of the paddles for generating freak waves when the initial water depths are $0.67\,m$ and $0.7\,m$ (Supplementary data for this figure can be found in Section 8)

.

studied experimentally and numerically. The time histories of the wave maker motions for cases with still water depths $H = 0.67\,m$ and $H = 0.7\,m$ are plotted in Figure 16, while the wave maker motion of $H = 0.65\,m$ is the same as the one in Figure 5. Supplementary data for these wave maker motions can be found in 8. Based on the numerical investigations in Section 5.2, both the δ^+SPH with TIC and the inclusion of the air phase are essential to simulate the whole process of freak wave slamming on a box-shape structure. Therefore, the multiphase δ^+SPH model is utilized from here on.

5.3.1. Still water depth $H = 0.65\,m$

The case of $H = 0.65\,m$ has a deck clearance of $0.0985\,m$, which is the maximum among the three cases. Figure 17 shows the wave profile snapshots. The plunging wave impacts on the structure and entraps an air bubble, which interacts with the incident wave and eventually disappears under the compression force exerted by the wave. The multiphase δ^+SPH model predicts the highly-deformed wave profiles during the whole slamming process with a good accuracy.

The wave impact pressure caused by the freak wave is an important factor to consider in the design, but is challenging to predict because of the high nonlinearity and the two-phase interaction nature. As discussed in Section 5.2.1, two impact peaks should occur on the front wall of the structure at the initial slamming stage. They are induced by the compression of the air bubble and the re-impingement of the wave when the bubble disappears, respectively. The experiment did record two peaks and the multiphase δ^+SPH model reproduces them generally well (see the top panels of Figure 18). The magnitude of the first peak shows some discrepancies. This is presumably attributed to the three-dimensional (3D) effect of the experiment, in which the entrapped air bubble breaks into small bubbles and forms water-air mixtures. The bubbly flow and the possibly associated cavitation effect can lead to large pressures and pressure oscillations. These physics, however, cannot be captured by the present 2D SPH model, and hence the first pressure peak shows some differences. Note that the measured pressure oscillation near the first peak is essentially different from the pressure fluctuations predicted by the single-phase SPH model presented in Section 5.2.1.

The wave impingement also induces large pressures on the platform bottom as depicted in the bottom panels of Figure 18. The present SPH model predicts

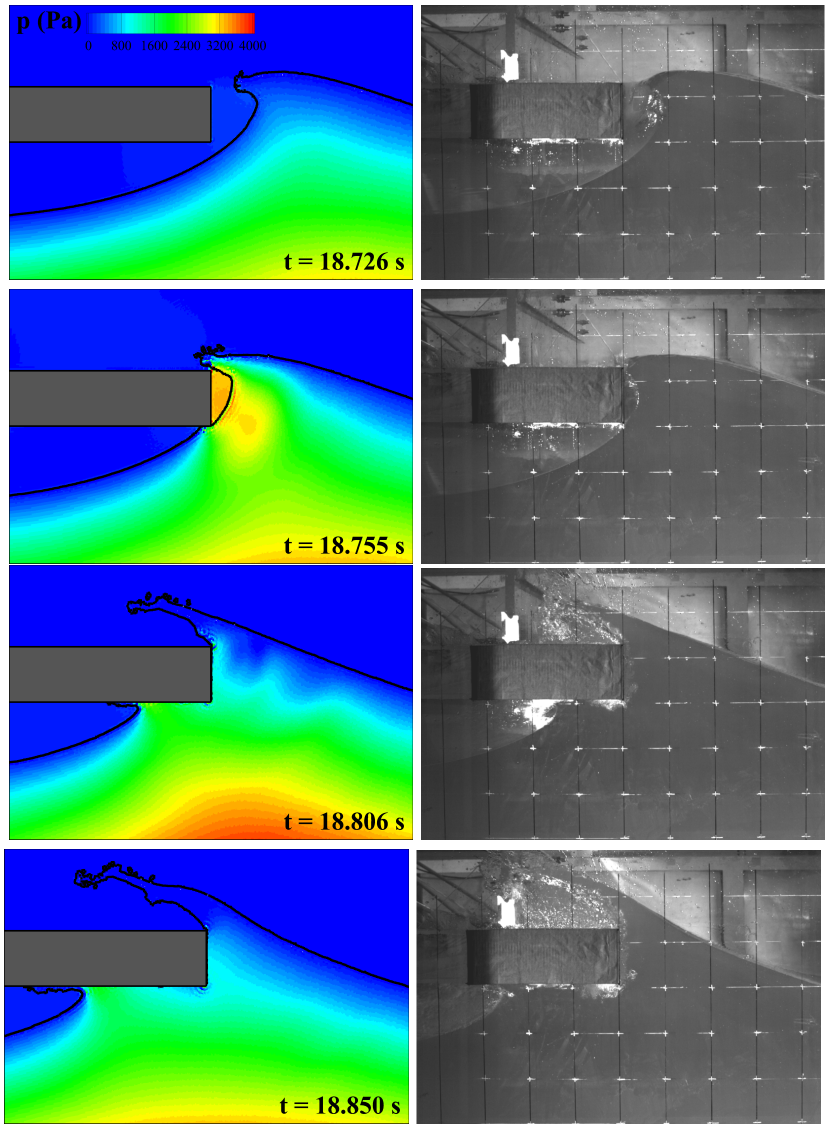

Figure 17: Wave profile snapshots for the freak wave case of $H = 0.65\,m$: multiphase δ^{+}SPH results (left column) and experimental measurements (right column).

the pressures at BP1 and BP2 fairly well, with a slight underestimation of the pressure magnitude at BP1. After the completion of the wave impingement when no significant impact pressures are applied on the structure (at about $t = 18.95\,s$), the subsequent wave-structure interaction resembles the water-exit process. Negative pressures are observed at the bottom wall in both the experiment and SPH simulation. Because of the relatively large deck clearance,

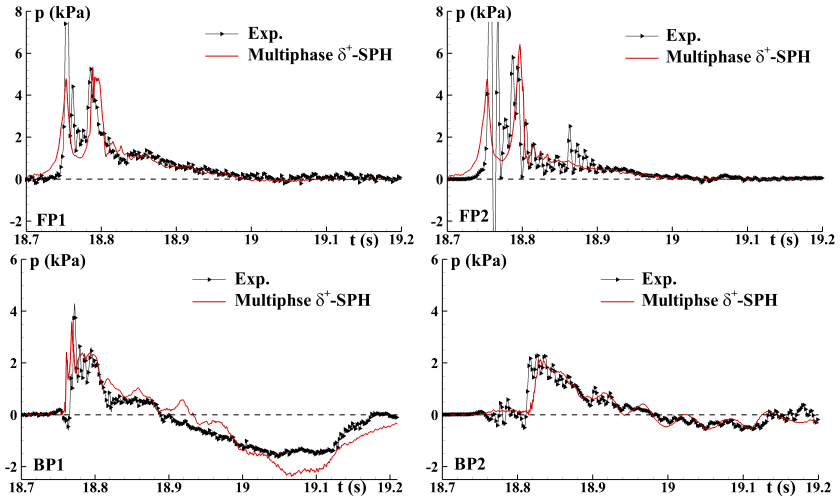

Figure 18: Wave impact pressures for the freak wave case of $H = 0.65\,m$: multiphase δ^+SPH results and experimental measurements.

the tongue of the wave does not impact on the top surface of the platform. Upon the wave-structure interaction, part of the incident wave turns up, forming a jet flow that goes up to the platform top (see the snapshots in Figure 17). The jet flow will fall down under gravity, becoming the green water.

5.3.2. Still water depth $H = 0.67\,m$

In the second freak wave case, the water depth is $H = 0.67\,m$ and the deck clearance is $0.0785\,m$. The wave slamming process predicted by the multiphase δ^+SPH model is compared against experimental snapshots in Figure 19 with good agreement. The wave impacts on the platform at the instant when the wave crest is in an almost upright shape. This wave front entraps less air than the previous case and therefore induces the impact with low-aeration which leads to short rise time and high peak pressure [7]. These characteristics are manifested in the experimental results of FP1 and FP2 (see Figure 20). The SPH simulation has predicted the impulse-like impact pressure (i.e. large peak and short rise time). The pressure peaks are comparable between the SPH results and experimental data and the negative pressure at the suction stage is well resolved (see BP1). The predicted pressure at FP2 does not exhibit the regular decaying process as shown in the experimental measurement. Similar to that discussed in the previous section, this can be attributed to the oscillations of bubbly flows which are not captured in the 2D SPH model. To investigate this, a 3D multiphase SPH simulation should be conducted in the future studies. In this case, the deck clearance is smaller than the previous case. Part of the wave crest directly impinges on the platform top and therefore the volume of green water increases (see Figure 19).

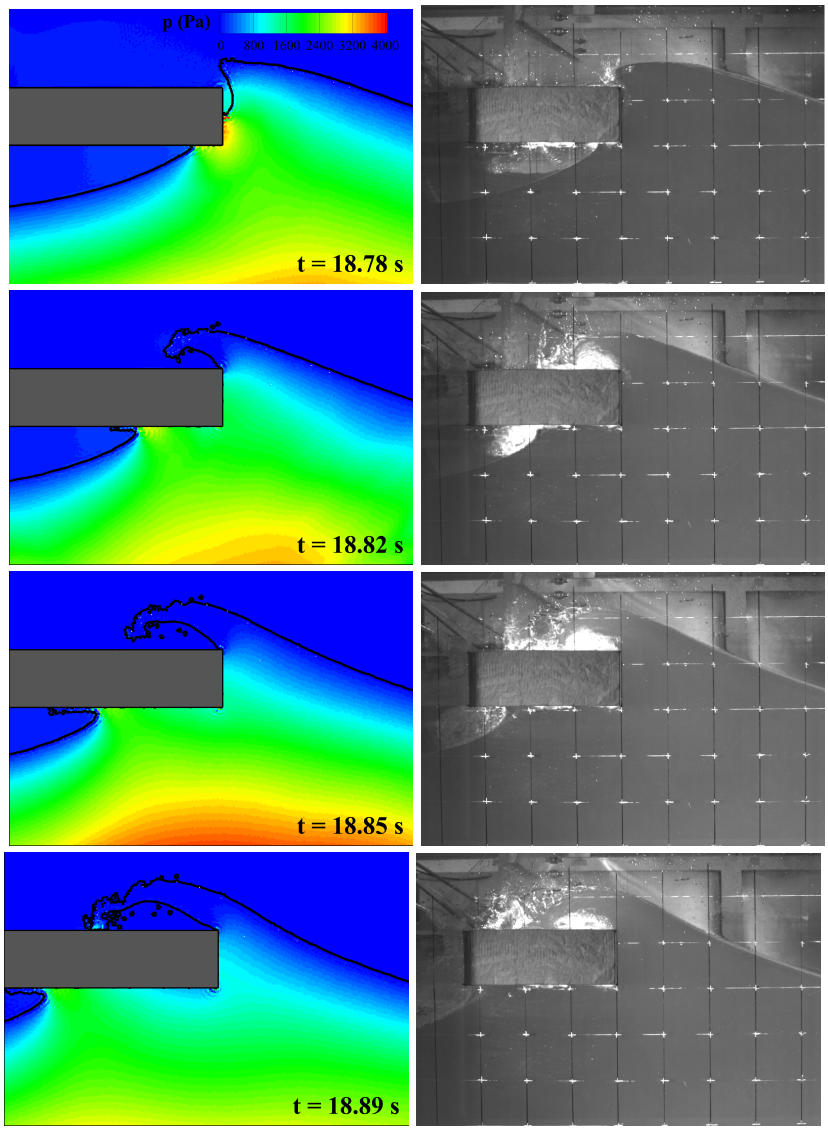

Figure 19: Wave profile snapshots for the freak wave case of $H = 0.67\,m$: multiphase δ^{+}SPH results (left column) and experimental measurements (right column).

5.3.3. Still water depth $H = 0.7\,m$

The third freak wave case has a water depth of $H = 0.7\,m$ and a deck clearance of $0.0485\,m$ (smallest among the three cases). Figure 21 presents the wave profiles at typical time instants. Due to the high water level, the crest of the plunging wave is higher than the top surface of the platform (see $t = 18.69\,s$). When the wave impact happens, the tongue of the plunging wave

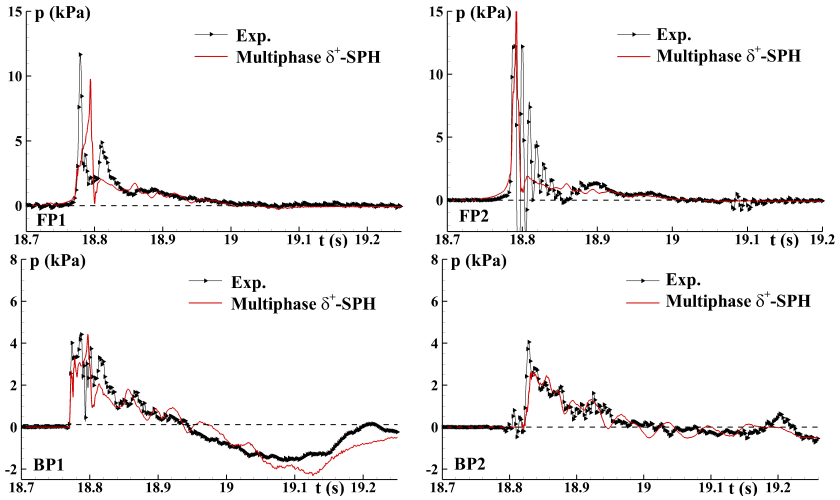

Figure 20: Wave impact pressures for the freak wave case of $H = 0.67\,m$: multiphase δ^+SPH results and experimental measurements.

overtops the platform, inducing massive green water. The multiphase δ^+SPH model has successfully captured the whole process of plunging breaker forming, rolling and impacting on the top of the deck and entrapping an air bubble. Indeed, during this process, the air phase plays an important role by imposing a negative pressure (see $t = 18.77\,s$) to force the water tongue quickly return to the top of the deck. The wave impact also causes large impact pressure on the vertical and bottom walls of the platform as presented in Figure 22. The pressure results at FP1 and FP2 are in a generally good agreement with the experiment data. Consistent with the freak wave cases of $H = 0.65\,m$ and $0.67\,m$, the SPH model slightly underestimates the pressure peaks because the 2D model misses some physics such as the bubbly flow. To further verify that, we compare the present FP1 result and that simulated by a 2D IBM method [73] in Figure 23. A good agreement is observed, showing the consistency of the 2D simulation results. Interestingly, the magnitude of the pressure at FP1 is smaller than that in the case of $H = 0.67\,m$. This is because, with a higher water level, FP1 is slightly below the region where the top part of the wave front directly impinges on. For the wave pressures on the bottom wall, i.e. BP1 and BP2, both positive and negative components are observed in the SPH results and the experimental data and a good agreement is achieved, being consistent with the previous two cases. The negative pressure is induced by the wave receding. A distinct phenomenon for the bottom pressure in this case is the low-frequency oscillation. The δ^+SPH model also captures these pressure oscillations, but the magnitude is slightly smaller. These pressure oscillations are presumably caused by the oscillations due to the flow separations near the sharp corners of the upstream walls, and the difference of the oscillating magnitudes between SPH and experimental results can be attributed to the three-dimensional effect of the wave-structure interaction. For a further investigation of the flow features

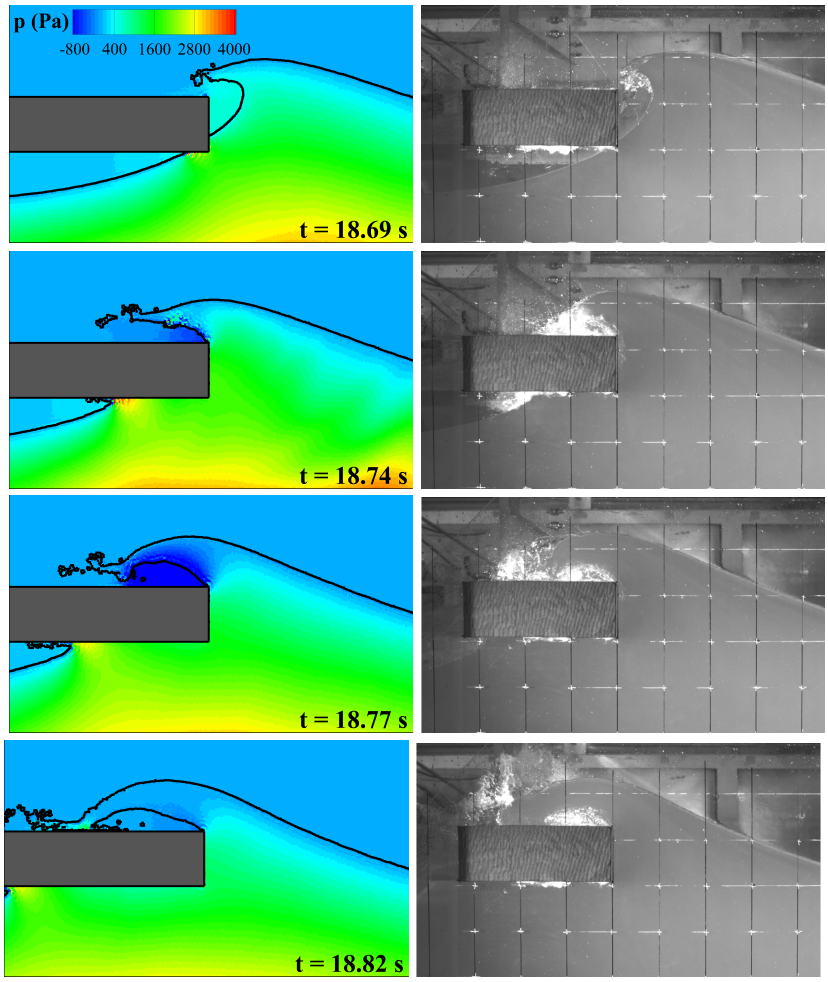

Figure 21: Wave profile snapshots for the freak wave case of $H = 0.7\,m$: multiphase δ^{+}SPH results (left column) and experimental measurements (right column). To clearly demonstrate the negative pressure, the minimum pressure value in the legend has been adjusted to -800 Pa.

around the platform, velocity fields at typical time instants are depicted in Figure 24. At the instant when the wave impact is about to happen, the crest of the plunging wave has large velocities and hence can induce large pressures when impinging on the structure (see $t = 18.66\,s$). From the snapshot at $t = 19.10\,s$, a flow rotation is clearly observed below the right corner of the platform. This rotating flow is induced by the flow separation near the structural corner. When the flow leaves that corner, violent splashes are generated due to the strong vertex (see the contour at $t = 19.19\,s$ and $t = 19.46\,s$). Afterwards, the wet surface on the platform bottom narrows as the free surfaces shrink from the two sides (see the last contour). It is worth mentioning that the wave-structure

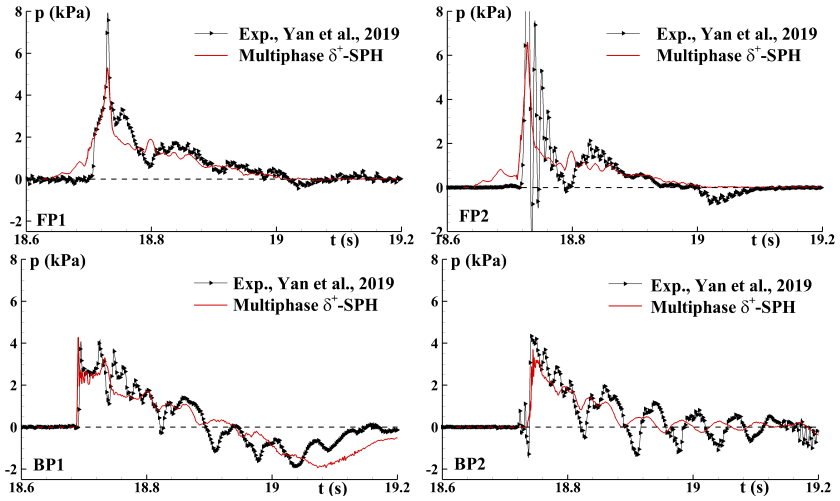

Figure 22: Wave impact pressures for the freak wave case of $H = 0.7\,m$: multiphase δ^{+}SPH results and experimental measurements.

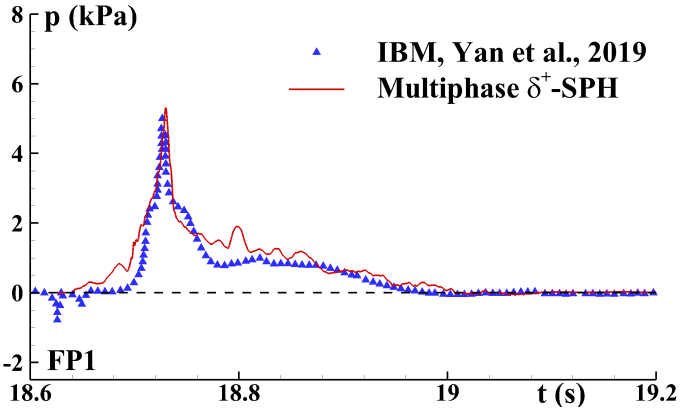

Figure 23: Multiphase SPH result compared with the IBM [73] result for the impact pressure at FP1.

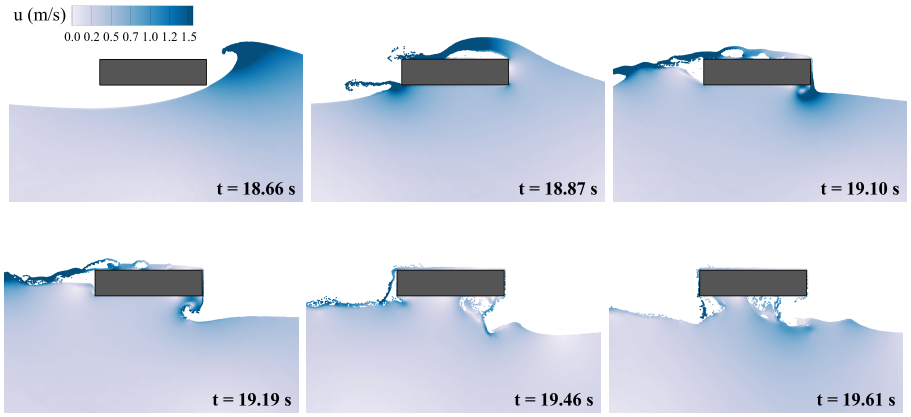

Figure 24: Contour of velocity magnitude at typical time instants during the freak wave impact in the case of $H = 0.7\,m$; Air particles are hidden to clearly demonstrate the velocity field in water.

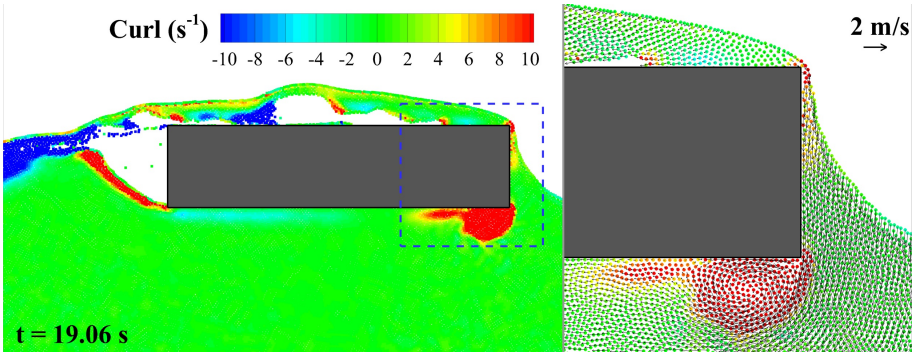

Figure 25: Vorticity field at $t = 19.06\,s$ after the freak wave impacts on the platform in the case of $H = 0.7\,m$; the sub-figure on the right side is an enlarged view for the flow detail around the right corners of the platform.

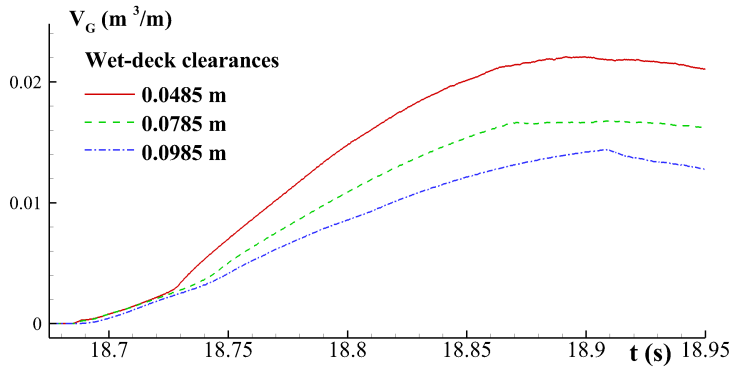

Figure 26: Evolutions of the green water volume in the cases with different wet-deck clearances.

interaction snapshots when the wave recedes from the structure and negative pressure happens are consistent with the experimental observations described in Figure 5 of [19].

To further illustrate the flow separation around the sharp corner, the vorticity field at $t = 19.06\,s$ is depicted in Figure 25 with an enlarged view showing the velocity vectors. As can be seen, a strong vortex is formed beneath the corner in which the fluid pressure is negative as indicated by BP1 in Figure 22. The zoom-in figure shows that, a uniform particle distribution is maintained around the sharp corner of the structure. The regularized particle distribution tightly attached to the platform wall is attributed to the particle shifting and tensile instability control as used in the δ^+SPH model. All the particles on the right side of the platform possess downward velocities. This shows the water-exit nature of the freak wave-structure interaction at this stage, among which the platform structure undergoes large suction forces from the wave.

6. Freak wave impact with different deck clearance

The wet-deck clearance plays an important role in affecting the wave impact force applied onto a platform structure and the green water volume, and is one of the key considerations in a real design. This section, therefore, studies how the deck clearance influences the green water and wave force in a freak-wave circumstance. Based on the freak wave case of $H = 0.7\,m$ and $H_{b1} = 0.7485\,m$ (the case in Section 5.3.3), other two more deck elevations are studied using the multiphase δ^+SPH model, i.e. $H_{b2} = 0.7785\,m$ and $H_{b3} = 0.7985\,m$. The deck clearances for the three cases are $d_1 = 0.0485\,m$, $d_2 = 0.0785\,m$ and $d_3 = 0.0985\,m$, respectively.

Figure 26 plots the green water volume during the wave impact process for the three deck-clearance cases. As can be seen, the volume of green water increases rapidly at the initial stage of each wave impact case, and reaches its maximum when the main body of the wave crest passes through the platform. The maximum volumes of green water in the three cases are $0.022\,m^3/m$,

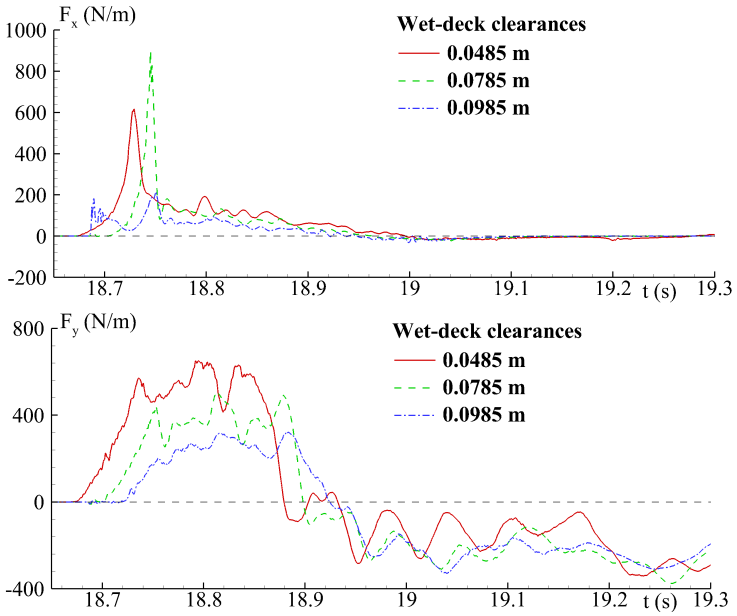

Figure 27: Evolutions of horizontal (F_x) and vertical (F_y) impact forces in the cases with different wet-deck clearances.

$0.017\,m^3/m$ and $0.014\,m^3/m$, respectively, in general reducing with the increase of the deck clearance.

Integrating the wave impact pressures on the platform structure leads to the wave impact forces along x and y directions, which are plotted in Figure 27. The wave, when first impacting on the platform, applies a large horizontal force along the wave propagation direction. The maximum horizontal impact force (of amplitude around 900 N/m) occurs in the case of $d_2 = 0.0785\,m$ since in this case the plunging wave crest impinges on the entire front wall. This force decays very quickly after the first wave impingement is over. In contrast, the vertical force lasts for the entire wave-structure interaction process. In addition, the vertical force changes its direction as the wave profile evolves. Particularly, the wave applies a positive lifting force at the initial wave impact stage until $t = 18.92\,s$. The wave-structure process at this stage corresponds to the water-entry phase categorized by [19]. After that, a negative force that pulls the structure down, i.e. the suction effect, is observed. This corresponds to the water-exit phase as discussed in [19]. The magnitudes of the suction forces in all three cases are comparable to the lifting forces, being consistent with the discussions in [6]. Different from the lifting force that withstands the gravity force of the structure, the suction force coincides the direction of the gravity force and hence increases the external force exerted on the structure, increasing the risk of structural damage. With the increase of the deck clearance, the positive vertical force at the water-entry phase reduces whereas the negative force shows slightly increasing trends. This is because the water-exit phenomenon is easier

to happen if the deck clearance is larger.

7. Conclusions and perspectives

The multiphase δ^+SPH model is applied in this work to simulate freak wave impacts on a fixed rectangular platform. A piston wave maker is implemented to simulate the physical wave maker motion and a viscous damping zone is added to minimize the wave reflection from the downstream boundary. Validated by our experimental studies of regular and freak waves, the δ^+SPH based numerical wave flume is capable of predicting the long-distance wave propagation without noticeable unphysical numerical dissipations. This is extremely advantageous in wave-structure interaction studies because the wave impact characteristics are highly dependent on the incident wave condition. In addition, the numerical wave flumes shows a good particle-size convergence. It is found that to reproduce the high-curvature crest of a plunging wave, a finer particle resolution is needed than that for the wave prediction at locations where the wave deformation and nonlinearity are smaller.

Results of the multiphase δ^+SPH model are validated by the experimental data. Good accuracy of the numerical model is demonstrated, especially in capturing the negative pressure in the latter stage of the wave slamming. The accuracy of the present δ^+SPH model is benefited from the nested particle shifting and tensile instability control techniques, without which the numerical results can be completely wrong due to the unphysical flow voids caused by tensile instability.

The highly-deformed wave profiles and violent impact pressures during the wave impact process are studied. At the initial stage of the wave slamming process, the wave approaches the structure, exerting large positive (compressive) pressures. This is analogy to the water-entry problem. An important phenomenon during this stage is the air entrapment that has been shown to affect the local wave impact characteristics significantly. It has been demonstrated that a multiphase simulation that takes the air phase into account is essential for a SPH model to accurately simulate this phenomenon. Specifically, the evolution of the air-water interface simulated by the multiphase δ^+SPH model agrees well with our experimental measurements and the impact pressures on the front and bottom walls of the platform structure are reasonably predicted.

Under gravity, the wave will tend to recede from the structure after a certain time, applying negative pressures that pull the structure down (resembles the water-exit of immersed structures). The suction-like negative pressures in the wave slamming process are simulated by SPH for the first time in this study. A comparison study demonstrates the importance of the tensile instability control in reproducing the negative pressure. Using the validated numerical model, the suction effects in three freak wave impact cases are studied. The magnitude of the negative pressure and the associated oscillations are accurately simulated in comparing with the experimental data. The interactions between the same incident wave with platforms (the same shape) of different elevations are also

studied. It is found that, with the decrease of the deck clearance, the green water volume and the positive lifting force increase whereas the negative suction force slightly reduces.

It has been found that the present 2D SPH model underestimates the impact pressures on the front wall slightly. This is presumably because the 3D wave motions and the associated bubbly flows that happen in reality cannot be captured by a 2D model. To explore the 3D effect in this particular wave slamming scenario, 3D SPH simulations with adaptive particle refinement will be conducted in the future studies. In addition, turbulence models (see, e.g., [18, 42]) should be introduced into the present δ^+SPH model to enhance the prediction of the turbulence features during the wave slamming process.

8. Supplementary material

See supplementary material for the paddle motion data to generate the regular and freak waves.

9. Acknowledgements

The author PengNan Sun is funded by a post-doctoral research grant from Ecole Centrale Nantes. Min Luo appreciates the Open Research Funding SKHL1710 and SKHL1712 from the State Key Laboratory of Hydraulics and Mountain River Engineering in Sichuan University. The experimental work was financially supported by the Singapore Maritime Institute and Sembcorp Marine Technology Pte Ltd (research grant SMI-2014-OF-02).

References

[1] Adami, S., Hu, X., Adams, N.A., 2012. A generalized wall boundary condition for smoothed particle hydrodynamics. Journal of Computational Physics 231, 7057–7075.

[2] Allsop, W., Vicinanza, D., McKenna, J., 1996. Wave forces on vertical and composite breakwaters .

[3] Altomare, C., Domínguez, J.M., Crespo, A., González-Cao, J., Suzuki, T., Gómez-Gesteira, M., Troch, P., 2017. Long-crested wave generation and absorption for SPH-based DualSPHysics model. Coastal Engineering 127, 37–54.

[4] Antuono, M., Colagrossi, A., Marrone, S., Lugni, C., 2011. Propagation of gravity waves through an SPH scheme with numerical diffusive terms. Computer Physics Communications 182, 866–877.

[5] Antuono, M., Colagrossi, A., Marrone, S., Molteni, D., 2010. Free-surface flows solved by means of SPH schemes with numerical diffusive terms. Computer Physics Communications 181, 532–549.

[6] Baarholm, R., 2001. Theoretical and Experimental Studies of Wave Impact underneath Decks of Offshore Structures. Ph.D. thesis. PhD thesis, Norwegian University of Science and Technology, Trondheim, Norway.

[7] Bullock, G., Obhrai, C., Peregrine, D., Bredmose, H., 2007. Violent breaking wave impacts. part 1: Results from large-scale regular wave tests on vertical and sloping walls. Coastal Engineering 54, 602–617.

[8] Cao, X.Y., Tao, L., Zhang, A.M., Ming, F.R., 2019. Smoothed particle hydrodynamics (SPH) model for coupled analysis of a damaged ship with internal sloshing in beam seas. Physics of Fluids 31, 032103.

[9] Chan, E.S., 1994. Mechanics of deep water plunging-wave impacts on vertical structures. Coastal engineering 22, 115–133.

[10] Chen, H.C., Yu, K., 2009. CFD simulations of wave–current-body interactions including greenwater and wet deck slamming. Computers & fluids 38, 970–980.

[11] Chen, L., Taylor, P.H., Draper, S., Wolgamot, H., 2019. 3-D numerical modelling of greenwater loading on fixed ship-shaped FPSOs. Journal of Fluids and Structures 84, 283–301.

[12] Chen, X., 2017. Development of three-dimensional numerical wave basin for simulation of extreme events in ocean. Ph.D. thesis. National University of Singapore, Singapore.

[13] Chuang, W.L., Chang, K.A., Mercier, R., 2018. Kinematics and dynamics of green water on a fixed platform in a large wave basin in focusing wave and random wave conditions. Experiments in Fluids 59, 100.

[14] Colagrossi, A., Antuono, M., Le Touzé, D., 2009. Theoretical considerations on the free-surface role in the smoothed-particle-hydrodynamics model. Physical Review E 79, 056701.

[15] Colagrossi, A., Antuono, M., Souto-Iglesias, A., Le Touzé, D., 2011. Theoretical analysis and numerical verification of the consistency of viscous smoothed-particle-hydrodynamics formulations in simulating free-surface flows. Physical Review E 84, 026705.

[16] Colagrossi, A., Landrini, M., 2003. Numerical Simulation of Interfacial Flows by Smoothed Particle Hydrodynamics 191, 448–475.

[17] Cooker, M.J., 2002. Liquid impact, kinetic energy loss and compressibility: Lagrangian, eulerian and acoustic viewpoints. Journal of engineering mathematics 44, 259–276.

[18] Di Mascio, A., Antuono, M., Colagrossi, A., Marrone, S., 2017. Smoothed particle hydrodynamics method from a large eddy simulation perspective. Physics of Fluids 29, 035102.

[19] Faltinsen, O.M., Landrini, M., Greco, M., 2004. Slamming in marine applications. Journal of Engineering Mathematics 48, 187–217.

[20] Gao, R., Ren, B., Wang, G., Wang, Y., 2012. Numerical modelling of regular wave slamming on subface of open-piled structures with the corrected SPH method. Applied Ocean Research 34, 173–186.

[21] Gómez-Gesteira, M., Cerqueiro, D., Crespo, C., Dalrymple, R., 2005. Green water overtopping analyzed with a SPH model. Ocean Engineering 32, 223–238.

[22] Gong, K., Liu, H., Wang, B.l., 2009. Water entry of a wedge based on SPH model with an improved boundary treatment. Journal of Hydrodynamics 21, 750–757.

[23] Gotoh, H., Khayyer, A., 2016. Current achievements and future perspectives for projection-based particle methods with applications in ocean engineering. Journal of Ocean Engineering and Marine Energy 2, 251–278.

[24] Gotoh, H., Khayyer, A., 2018. On the state-of-the-art of particle methods for coastal and ocean engineering. Coastal Engineering Journal 60, 79–103.

[25] Hurricane-Ivan, 2004. `http://members.home.nl/the_sims/rig/h-ivan.htm`.

[26] Hurricane-Katrina, 2005. Oil spills, ravaged industry and lost islands add to the hurricane's toll. `https://www.theguardian.com/world/2005/sep/09/hurricanekatrina.usa1`.

[27] Khayyer, A., Gotoh, H., Shimizu, Y., 2017. Comparative study on accuracy and conservation properties of two particle regularization schemes and proposal of an optimized particle shifting scheme in ISPH context. Journal of Computational Physics 332, 236–256.

[28] Khayyer, A., Gotoh, H., Shimizu, Y., 2019. A projection-based particle method with optimized particle shifting for multiphase flows with large density ratios and discontinuous density fields. Computers & Fluids 179, 356–371.

[29] Khayyer, A., Gotoh, H., Shimizu, Y., Gotoh, K., Falahaty, H., Shao, S., 2018. Development of a projection-based sph method for numerical wave flume with porous media of variable porosity. Coastal Engineering 140, 1–22.

[30] Le Touzé, D., Colagrossi, A., Colicchio, G., Greco, M., 2013. A critical investigation of smoothed particle hydrodynamics applied to problems with free-surfaces. International Journal for Numerical Methods in Fluids 73, 660–691.

[31] Lesser, M., Field, J., 1983. The impact of compressible liquids. Annual review of fluid mechanics 15, 97–122.

[32] Lin, P., Liu, P.L.F., 1998. A numerical study of breaking waves in the surf zone. Journal of fluid mechanics 359, 239–264.

[33] Lind, S., Xu, R., Stansby, P., Rogers, B., 2012. Incompressible smoothed particle hydrodynamics for free-surface flows: A generalised diffusion-based algorithm for stability and validations for impulsive flows and propagating waves. Journal of Computational Physics 231, 1499–1523.

[34] Liu, M., Liu, G., 2010. Smoothed particle hydrodynamics (SPH): an overview and recent developments. Archives of computational methods in engineering 17, 25–76.

[35] Luo, M., Koh, C.G., 2017. Modelling of extreme wave impact on a fixed platform, in: The 27th International Ocean and Polar Engineering Conference, International Society of Offshore and Polar Engineers.

[36] Ma, Y., Dong, G., Perlin, M., Liu, S., Zang, J., Sun, Y., 2009. Higher-harmonic focused-wave forces on a vertical cylinder. Ocean Engineering 36, 595–604.

[37] Madsen, P.A., Schäffer, H., 2006. A discussion of artificial compressibility. Coastal engineering 53, 93–98.

[38] Marrone, S., Antuono, M., Colagrossi, A., Colicchio, G., Le Touzé, D., Graziani, G., 2011. Delta-SPH model for simulating violent impact flows. Computer Methods in Applied Mechanics and Engineering 200, 1526–1542.

[39] Marrone, S., Colagrossi, A., Antuono, M., Colicchio, G., Graziani, G., 2013. An accurate SPH modeling of viscous flows around bodies at low and moderate Reynolds numbers. Journal of Computational Physics 245, 456–475.

[40] Marrone, S., Colagrossi, A., Di Mascio, A., Le Touzé, D., 2015. Prediction of energy losses in water impacts using incompressible and weakly compressible models. Journal of Fluids and Structures 54, 802–822.

[41] Marrone, S., Colagrossi, A., Park, J., Campana, E., 2017. Challenges on the numerical prediction of slamming loads on lng tank insulation panels. Ocean Engineering 141, 512–530.

[42] Meringolo, D.D., Marrone, S., Colagrossi, A., Liu, Y., 2019. A dynamic δ-sph model: How to get rid of diffusive parameter tuning. Computers & Fluids 179, 334–355.

[43] Moghimi, M.H., Quinlan, N.J., 2019. Application of background pressure with kinematic criterion for free surface extension to suppress non-physical voids in the finite volume particle method. Engineering Analysis with Boundary Elements 106, 126–138.

[44] Mokos, A., Rogers, B.D., Stansby, P.K., 2017. A multi-phase particle shifting algorithm for SPH simulations of violent hydrodynamics with a large number of particles. Journal of Hydraulic Research 55, 143–162.

[45] Monaghan, J., Gingold, R., 1983. Shock Simulation by the particle method SPH. Journal of Computational Physics 52, 374–389.

[46] Monaghan, J.J., 1994. Simulating free surface flows with sph. Journal of computational physics 110, 399–406.

[47] Monaghan, J.J., 2000. SPH without a tensile instability. Journal of Computational Physics 159, 290–311.

[48] Oger, G., Doring, M., Alessandrini, B., Ferrant, P., 2007. An improved sph method: Towards higher order convergence. Journal of Computational Physics 225, 1472–1492.

[49] Oger, G., Marrone, S., Le Touzé, D., De Leffe, M., 2016. SPH accuracy improvement through the combination of a quasi-Lagrangian shifting transport velocity and consistent ALE formalisms. Journal of Computational Physics 313, 76–98.

[50] Park, H., Do, T., Tomiczek, T., Cox, D.T., van de Lindt, J.W., 2018. Numerical modeling of non-breaking, impulsive breaking, and broken wave interaction with elevated coastal structures: Laboratory validation and inter-model comparisons. Ocean Engineering 158, 78–98.

[51] Qin, H., Tang, W., Xue, H., Hu, Z., 2017. Numerical study of nonlinear freak wave impact underneath a fixed horizontal deck in 2-D space. Applied Ocean Research 64, 155–168.

[52] Rabczuk, T., Belytschko, T., Xiao, S., 2004. Stable particle methods based on Lagrangian kernels. Computer methods in applied mechanics and engineering 193, 1035–1063.

[53] Randles, P., Libersky, L.D., 1996. Smoothed particle hydrodynamics: some recent improvements and applications. Computer methods in applied mechanics and engineering 139, 375–408.

[54] Ren, B., He, M., Dong, P., Wen, H., 2015. Nonlinear simulations of wave-induced motions of a freely floating body using WCSPH method. Applied Ocean Research 50, 1–12.

[55] Shadloo, M., Oger, G., Le Touzé, D., 2016. Smoothed particle hydrodynamics method for fluid flows, towards industrial applications: Motivations, current state, and challenges. Computers & Fluids 136, 11–34.

[56] Shao, S., Ji, C., Graham, D.I., Reeve, D.E., James, P.W., Chadwick, A.J., 2006. Simulation of wave overtopping by an incompressible SPH model. Coastal engineering 53, 723–735.

[57] Sun, P., Colagrossi, A., Le Touzé, D., Zhang, A.M., 2019a. Extension of the δ-plus-sph model for simulating Vortex-Induced-Vibration problems. Journal of Fluids and Structures 90, 19–42.

[58] Sun, P., Colagrossi, A., Marrone, S., Antuono, M., Zhang, A.M., 2019b. A consistent approach to particle shifting in the δ-plus-sph model. Computer Methods in Applied Mechanics and Engineering 348, 912–934.

[59] Sun, P., Colagrossi, A., Marrone, S., Zhang, A., 2017. The δplus-SPH model: Simple procedures for a further improvement of the SPH scheme. Computer Methods in Applied Mechanics and Engineering 315, 25–49.

[60] Sun, P., Ming, F., Zhang, A., 2015. Numerical simulation of interactions between free surface and rigid body using a robust SPH method. Ocean Engineering 98, 32–49.

[61] Sun, P., Zhang, A.M., Marrone, S., Ming, F., 2018a. An accurate and efficient SPH modeling of the water entry of circular cylinders. Applied Ocean Research 72, 60–75.

[62] Sun, P.N., Colagrossi, A., Marrone, S., Antuono, M., Zhang, A.M., 2018b. Multi-resolution Delta-plus-SPH with tensile instability control: towards high reynolds number flows. Computer Physics Communications 224, 63–80.

[63] Sun, P.N., Le Touzé, D., Zhang, A.M., 2019c. Study of a complex fluid-structure dam-breaking benchmark problem using a multi-phase sph method with apr. Engineering Analysis with Boundary Elements 104, 240–258.

[64] Sun, P.N., Ming, F.R., Zhang, A.M., Wang, B., 2019d. Viscous flow past a NACA0012 foil below a free surface through the delta-plus-SPH method. International Journal of Computational Methods 16, 1846007.

[65] Tafuni, A., Domínguez, J., Vacondio, R., Crespo, A., 2018. A versatile algorithm for the treatment of open boundary conditions in smoothed particle hydrodynamics GPU models. Computer Methods in Applied Mechanics and Engineering 342, 604–624.

[66] Tran-Duc, T., Phan-Thien, N., Khoo, B.C., 2017. A smoothed particle hydrodynamics (sph) study of sediment dispersion on the seafloor. Physics of Fluids 29, 083302.

[67] Tran-Duc, T., Phan-Thien, N., Khoo, B.C., 2018. A smoothed particle hydrodynamics (sph) study on polydisperse sediment from technical activities on seabed. Physics of Fluids 30, 023302.

[68] Violeau, D., Rogers, B.D., 2016. Smoothed particle hydrodynamics (SPH) for free-surface flows: past, present and future. Journal of Hydraulic Research 54, 1–26.

[69] Wang, D., Shao, S., Li, S., Shi, Y., Arikawa, T., Zhang, H., 2018. 3D ISPH erosion model for flow passing a vertical cylinder. Journal of Fluids and Structures 78, 374–399.

[70] Wen, H., Ren, B., Dong, P., Wang, Y., 2016. A SPH numerical wave basin for modeling wave-structure interactions. Applied Ocean Research 59, 366–377.

[71] Wendland, H., 1995. Piecewise polynomial, positive definite and compactly supported radial functions of minimal degree. Adv. Comput. Math. 4, 389–396.

[72] Xue, M.A., Lin, P., 2011. Numerical study of ring baffle effects on reducing violent liquid sloshing. Computers & Fluids 52, 116–129.

[73] Yan, B., Luo, M., Bai, W., 2019. An experimental and numerical study of plunging wave impact on a box-shape structure. Marine Structures 66, 272–287.

[74] Ye, T., Pan, D., Huang, C., Liu, M., 2019. Smoothed particle hydrodynamics (SPH) for complex fluid flows: Recent developments in methodology and applications. Physics of Fluids 31, 011301.

[75] Zhang, A., Sun, P., Ming, F., Colagrossi, A., 2017. Smoothed particle hydrodynamics and its applications in fluid-structure interactions. Journal of Hydrodynamics, Ser. B 29, 187–216.

[76] Zhang, Z.L., Liu, M.B., 2018. A decoupled finite particle method for modeling incompressible flows with free surfaces. Applied Mathematical Modelling 60, 606–633.